

Solar Winds Driven by Nonlinear Low-Frequency Alfvén Waves from the Photosphere : Parametric Study for Fast/Slow Winds and Disappearance of Solar Winds

Takeru K. Suzuki¹ & Shu-ichiro Inutsuka

Department of Physics, Kyoto University, Kitashirakawa, Kyoto, 606-8502, Japan

Abstract. We investigate how properties of the corona and solar wind in open coronal holes depend on properties of magnetic fields and their footpoint motions at the surface. We perform one-dimensional magnetohydrodynamical (MHD) simulations for the heating and the acceleration in coronal holes by low-frequency Alfvén waves from the photosphere to 0.3 or 0.1AU. We impose low-frequency ($\lesssim 0.05\text{Hz}$) transverse fluctuations of the field lines at the photosphere with various amplitude, spectrum, and polarization in the open flux tubes with different photospheric field strength, $B_{r,0}$, and super-radial expansion of the cross section, f_{max} . We find that transonic solar winds are universal consequences. The atmosphere is also stably heated up to $\gtrsim 10^6\text{K}$ by the dissipation of the Alfvén waves through compressive-wave generation and wave reflection in the cases of the sufficient wave input with photospheric amplitude, $\langle dv_{\perp,0} \rangle \gtrsim 0.7\text{km s}^{-1}$. The density, and accordingly the mass flux, of solar winds show a quite sensitive dependence on $\langle dv_{\perp,0} \rangle$ because of an unstable aspect of the heating by the nonlinear Alfvén waves. A case with $\langle dv_{\perp,0} \rangle = 0.4\text{km s}^{-1}$ gives $\simeq 50$ times smaller mass flux than the fiducial case for the fast wind with $\langle dv_{\perp,0} \rangle = 0.7\text{km s}^{-1}$; solar wind *virtually disappears* only if $\langle dv_{\perp,0} \rangle$ becomes $\simeq 1/2$. We also find that the solar wind speed has a positive correlation with $B_{r,0}/f_{\text{max}}$, which is consistent with recent observations by Kojima et al. Based on these findings, we show that both fast and slow solar winds can be explained by the single process, the dissipation of the low-frequency Alfvén waves, with different sets of $\langle dv_{\perp,0} \rangle$ and $B_{r,0}/f_{\text{max}}$. Our simulations naturally explain the observed (i) anti-correlation of the solar wind speed and the coronal temperature and (ii) larger amplitude of Alfvénic fluctuations in the fast wind. In Appendix, we also explain our implementation of the outgoing boundary condition of the MHD waves with some numerical tests.

1. Introduction

The corona can be roughly divided into two sectors with respect to magnetic field configurations on the solar surface. One is closed field regions in which both footpoints of each field line are rooted at the photosphere. The other is open field regions in which one footpoint is anchored at the photosphere and the other is open into the interplanetary space. The open field regions roughly coincide with areas called coronal holes which are dark in X-rays. From the coronal holes, the hot plasma streams out as solar winds.

The Alfvén wave, generated by the granulations or other surface activities, is a promising candidate operating in the heating and acceleration of solar winds from coronal holes. It can travel a long distance so that the dissipation plays a role in the heating of the solar wind plasma as well as the lower coronal plasma, in contrast to other processes, such as magnetic reconnection events and compressive waves, the heating of which probably concentrates at lower altitude. High-frequency ($\sim 10^4\text{Hz}$) ioncyclotron waves were recently suggested for the inferred preferential heating of the perpendicular temperature of the heavy ions [Axford & McKenzie, 1997; Kohl et al., 1998], whereas there is still a possibility that the observed temperature anisotropy might be due to a line-of-sight effect [Raouafi & Solanki, 2004]. However, the protons which compose the main part of the plasma are supposed to be mainly heated

by low-frequency ($\lesssim 0.1\text{Hz}$) components in the magnetohydrodynamical (MHD) regime. This is first because the low-frequency wave is expected to have more power, and second because the resonance frequency of the proton is higher than those of heavier ions so that the energy of the ioncyclotron wave is in advance absorbed by the heavy ions [Cranmer, 2000].

The treatment of the wave dissipation is quite complicated even for MHD processes. The main reason is that the nonlinearity becomes essential because amplitudes of upgoing waves are inevitably amplified in the stratified atmosphere with decreasing density. Therefore, numerical simulation is a powerful tool; there are several works on the wave propagation and dissipation in one-dimensional (1D) [Lau & Sireger, 1996; Kudoh & Shibata, 1999; Orta et al., 2003] and in two-dimensional [Ofman & Davila, 1997, 1998; Ofman, 2004] simulations. However, large density contrast amounting more than 15 orders of magnitude from the photosphere to the outer heliosphere has prevented one so far from carrying out numerical simulation in a broad region from the photosphere to the interplanetary space even in 1D modeling.

In Suzuki & Inutsuka [2005] (paper I hereafter) we successfully carried out 1D MHD simulation with radiative cooling and thermal conduction from the photosphere to 0.3 AU. We showed that the coronal heating and the fast solar wind acceleration in the coronal hole are natural consequences of the transverse footpoint fluctuations of the magnetic field lines. Low-frequency ($\lesssim 0.05\text{Hz}$) Alfvén waves are generated by the photospheric fluctuations [Ulrich, 1996; Cranmer & van Ballegoijen, 2005]. The sufficient amount of the energy transmits into the corona in spite of attenuation in the chromosphere and the transition region (TR), so that they effectively dissipate to heat and accelerate the coronal plasma. Although it is based on the one-fluid MHD approximation, it, for

¹JSPS Research Fellow; Present address : Graduate School of Arts & Sciences, University of Tokyo, Meguro, Tokyo, 153-8902, Japan

the first time, self-consistently treats the plasma heating and the propagation of the Alfvén waves from the photosphere to the interplanetary space. However, we studied only one case for the fast solar wind in paper I. It is important to examine how properties of the corona and the solar wind are affected by adopting different types of the wave injections and/or different magnetic field geometry of the flux tubes. The purpose of this paper is to study parametrically the heating by the low-frequency Alfvén waves.

In this paper we adopt the one-fluid MHD approximation in 1D flux tubes, which is the same as in paper I. This assumption is not strictly correct in the solar wind plasma, which will be discussed later (§6.2). However, we think that the MHD approximation is appropriate for studies of the average properties of the plasma in the corona and the solar wind because the plasma particles are sufficiently randomized by the fluctuating magnetic fields.

2. Simulation Set-up

We consider 1D open flux tubes which are super-radially open, measured by heliocentric distance, r . The simulation regions are from the photosphere ($r = 1R_\odot$) with density, $\rho = 10^{-7} \text{g cm}^{-3}$, to $65R_\odot$ (0.3AU) or $\simeq 20R_\odot$ ($\simeq 0.1\text{AU}$), where R_\odot is the solar radius. Radial field strength, B_r , is given by conservation of magnetic flux as

$$B_r r^2 f(r) = \text{const.}, \quad (1)$$

where $f(r)$ is a super-radial expansion factor. We adopt the same function as in Kopp & Holzer [1976] for $f(r)$ but consider two-step expansions:

$$f(r) = \frac{f_{1,\text{max}} \exp(\frac{r-R_1}{\sigma_1}) + f_1}{\exp(\frac{r-R_1}{\sigma_1}) + 1} \frac{f_{2,\text{max}} \exp(\frac{r-R_2}{\sigma_2}) + f_2}{\exp(\frac{r-R_2}{\sigma_2}) + 1}$$

where $f_1 = 1 - (f_{1,\text{max}} - 1) \exp(\frac{R_\odot - R_1}{\sigma_1})$ and $f_2 = 1 - (f_{2,\text{max}} - 1) \exp(\frac{R_\odot - R_2}{\sigma_2})$. The flux tube initially expands by a factor of $f_{1,\text{max}}$ around $R_1 = 1.01R_\odot$ corresponding to the 'funnel' structure [Tu et al., 2005], and followed by $f_{2,\text{max}}$ times expansion around $R_2 = 1.2R_\odot$ due to the large scale dipole magnetic fields (Figure 1). We define the total super-radial expansion as $f_{\text{max}} = f_{1,\text{max}} f_{2,\text{max}}$.

We prescribe the transverse fluctuations of the field line by the granulations at the photosphere, which excite Alfvén waves. We study cases of various spectra, polarizations, and root mean squared (rms) amplitudes, $\langle dv_{\perp,0} \rangle (\equiv \sqrt{\langle dv_{\perp,0}^2 \rangle}) (\text{km s}^{-1})$. $\langle dv_{\perp,0} \rangle$ and

power spectrum, $P(\nu) (\text{erg g}^{-1} \text{Hz}^{-1})$, have a relation of

$$\langle dv_{\perp,0}^2 \rangle = \int_{\nu_{\text{low cut}}^{\text{up}}}^{\nu_{\text{up cut}}^{\text{cut}}} P(\nu) d\nu. \quad (2)$$

The parameters adopted in different simulation Runs are tabulated in Table 1. We consider three types of spectrum : (i) $P(\nu) \propto \nu^{-1}$ (ii) $P(\nu) \propto \nu^0$ (white noise) (iii) $P(\nu) \propto \delta(1/\nu - 180\text{s})$ (sinusoidal waves with a period of 180 seconds) . For the first and second cases we set $\nu_{\text{low cut}} = 6 \times 10^{-4} \text{Hz}$ (a period of $\simeq 28\text{min}$) and $\nu_{\text{up cut}} = 0.05 \text{Hz}$ (20s) for Run I or $\nu_{\text{up cut}} = 0.025 \text{Hz}$ (40s) for the others. For the linearly polarized perturbations we only take into account one transverse component besides the radial component, while we consider the two transverse components for the circularly polarized case. Values of $\langle dv_{\perp,0} \rangle$ are chosen to be compatible with the observed photospheric velocity amplitude $\sim 1 \text{km s}^{-1}$ [Holweger et al., 1978]. At the outer boundaries, non-reflecting condition is imposed for all the MHD waves (see Appendix), which enables us to carry out simulations for a long time until quasi-steady state solutions are obtained without unphysical wave reflection.

We dynamically treat the propagation and dissipation of the waves and the heating and acceleration of the plasma by solving ideal MHD equations with the relevant physical processes (paper I):

$$\frac{d\rho}{dt} + \frac{\rho}{r^2 f} \frac{\partial}{\partial r} (r^2 f v_r) = 0, \quad (3)$$

$$\rho \frac{dv_r}{dt} = -\frac{\partial p}{\partial r} - \frac{1}{8\pi r^2 f} \frac{\partial}{\partial r} (r^2 f B_\perp^2) + \frac{\rho v_\perp^2}{2r^2 f} \frac{\partial}{\partial r} (r^2 f) - \rho \frac{GM_\odot}{r^2}, \quad (4)$$

$$\rho \frac{d}{dt} (r \sqrt{f} v_\perp) = \frac{B_r}{4\pi} \frac{\partial}{\partial r} (r \sqrt{f} B_\perp). \quad (5)$$

$$\rho \frac{d}{dt} \left(e + \frac{v^2}{2} + \frac{B^2}{8\pi\rho} - \frac{GM_\odot}{r} \right) + \frac{1}{r^2 f} \frac{\partial}{\partial r} \left[r^2 f \left\{ \left(p + \frac{B^2}{8\pi} \right) v_r - \frac{B_r}{4\pi} (\mathbf{B} \cdot \mathbf{v}) \right\} \right] + \frac{1}{r^2 f} \frac{\partial}{\partial r} (r^2 f F_c) + q_R = 0, \quad (6)$$

$$\frac{\partial B_\perp}{\partial t} = \frac{1}{r \sqrt{f}} \frac{\partial}{\partial r} [r \sqrt{f} (v_\perp B_r - v_r B_\perp)], \quad (7)$$

where ρ , \mathbf{v} , p , \mathbf{B} are density, velocity, pressure, and magnetic field strength, respectively, and subscripts r and \perp denote radial and tangential components; $\frac{d}{dt}$ and $\frac{\partial}{\partial t}$ denote Lagrangian and Eulerian

Table 1. Model Parameters

Run	I	II	III	IV	V			
Outer Bound.	$65R_\odot$	$20R_\odot$	$20R_\odot$	$20R_\odot$	$20R_\odot$			
Spectrum	ν^{-1}	ν^{-1}	ν^0	$\delta(\nu^{-1} - 180\text{s})$	$\delta(\nu^{-1} - 180\text{s})$			
Polarization	Linear	Linear	Linear	Linear	Circular			
$\langle dv_{\perp,0} \rangle (\text{km/s})$	0.7	0.7	0.7	0.7	0.7			
$B_{r,0} (\text{G})$	161	161	161	161	161			
$f_{1,\text{max}}$	30	30	30	30	30			
$f_{2,\text{max}}$	2.5	2.5	2.5	30	2.5			
Description	Fast Wind (paper I)	Coarse Ver. of Run I						
				VI	VII	VIII	IX	X
				$20R_\odot$	$20R_\odot$	$22R_\odot$	$20R_\odot$	$65R_\odot$
				ν^{-1}	ν^{-1}	ν^{-1}	ν^{-1}	ν^{-1}
				Linear	Linear	Linear	Linear	Linear
				1.4	0.4	0.7	0.3	1.0
				161	161	322	161	322
				30	30	45	30	45
				2.5	2.5	10	2.5	10
							No Steady State	Slow Wind

derivatives, respectively; $e = \frac{1}{\gamma-1} \frac{p}{\rho}$ is specific energy and we assume the equation of state for ideal gas with a ratio of specific heat, $\gamma = 5/3$; G and M_\odot are the gravitational constant and the solar mass; $F_c (= \kappa_0 T^{5/2} \frac{dT}{dr})$ is thermal conductive flux by Coulomb collisions, where $\kappa_0 = 10^{-6}$ in c.g.s unit [Braginskii, 1965]; q_R is radiative cooling described below. We use optically thin radiative loss [Landini & Monsignori-Fossi, 1990] in the corona and upper TR where temperature, $T \geq 4 \times 10^4$ K. In the chromosphere and low TR, we adopt empirical radiative cooling based on the observations [Anderson & Athay, 1989; Moriyasu et al., 2004] to take into account the optically thick effect. In the low chromosphere, the temperature sometimes drops to ~ 3000 K because we do not consider other heating sources, such as sound waves, which must be important there besides Alfvén waves [Carlsson & Stein, 1992; Bogdan et al., 2003]. Such unrealistically low temperature interrupts the propagation of the Alfvén waves in the low chromosphere through the change of the density structure. To give realistic estimates of the transmission of the Alfvén waves there, we switch off the radiative cooling, if the temperature becomes < 5000 K only when $\rho > 10^{-11} \text{ g cm}^{-3}$.

We adopt the second-order MHD-Godunov-MOCCT scheme (Sano & Inutsuka 2006) to update the physical quantities. We solve eqs. (3)–(6) on fixed Eulerian mesh by remapping the physical variables updated in Lagrangian coordinate onto the original grids at each time step. The induction equation (7) is solved on the Eulerian grids. We use implicit time steps for the thermal conduction and radiative cooling in energy equation (6) because the Courant conditions are severe for these processes, while explicit time steps are adopted for the other terms. Each cell boundary is treated as discontinuity, and for the time evolution we solve nonlinear Riemann shock tube problems with the magnetic pressure term by using the Rankin-Hugoniot relations. Therefore, entropy generation, namely heating, is automatically calculated from the shock jump condition. A great advantage of our code is that no artificial viscosity is required even for strong MHD shocks; numerical diffusion is suppressed to the minimum level for adopted numerical resolution.

We initially set static atmosphere with a temperature $T = 10^4$ K to see whether the atmosphere is heated up to coronal temperature and accelerated to accomplish the transonic flow. At $t = 0$ we start to inject of the transverse fluctuations from the photosphere and continue the simulations until the quasi-steady states are achieved.

3. Heating and Acceleration by Wave Dissipation

Before showing results of the various coronal holes, we explain how the coronal heating and the solar wind acceleration were accomplished in the fiducial case (Run I) which was studied in paper I for the fast solar wind. Figure 2 plots the initial condition (dashed lines) and the results after the quasi-steady state condition is achieved at $t = 2573$ minutes (solid lines) in Run I, compared with recent observations of fast solar winds. From top to bottom, v_r (km s $^{-1}$), T (K), mass density, ρ (g cm $^{-3}$), and rms transverse amplitude, $\langle dv_\perp \rangle$ (km s $^{-1}$) are plotted. As for the density, we compare our result with observed electron density, N_e , in the corona. When deriving N_e from ρ in the corona, we assume H and He are fully ionized, and N_e (cm $^{-3}$) = $6 \times 10^{23} \rho$ (g cm $^{-3}$). These variables are averaged for 3 minutes to incorporate observational exposure time.

Figure 2 shows that the initially cool and static atmosphere is effectively heated and accelerated by the dissipation of the Alfvén waves. The sharp TR which divides the cool chromosphere with $T \sim 10^4$ K and the hot corona with $T \sim 10^6$ K is formed owing to a thermally unstable region around $T \sim 10^5$ K in the radiative cooling function [Landini & Monsignori-Fossi, 1990]. The hot corona streams out as the transonic solar wind. The simulation naturally explains the observed trend quite well. (see paper I for more detailed discussions.)

Figure 3 shows transfer of the energy (upper) and momentum (lower) flux of various components described below. The energy equation in an Eulerian form becomes

$$\frac{\partial E}{\partial t} + \nabla \cdot \mathbf{F} + L_{\text{loss}} = 0,$$

where E and \mathbf{F} are the total energy density and flux. $-L_{\text{loss}}$ is loss of the energy. For the analyses of quasi-steady state behaviors, we can reasonably assume that the time-average of the first term equals to 0. Then, in our case the explicit form becomes

$$\frac{1}{r^2 f} \frac{\partial}{\partial r} \left[r^2 f \left\langle \rho v_r \left(\frac{v_r^2 + v_\perp^2}{2} + e + \frac{p}{\rho} - \frac{GM_\odot}{r} \right) + \frac{B_\perp^2}{4\pi} v_r - \frac{B_r B_\perp v_\perp}{4\pi} + F_c \right\rangle \right] + \langle q_R \rangle = 0, \quad (8)$$

where $\langle \cdot \rangle$ denotes the time-average. Using the relation, $v_\perp = -B_\perp / \sqrt{4\pi\rho}$, for the outgoing Alfvén wave, we can extract the energy flux of the Alfvén wave from eq.(8) as follows [Jacques, 1977]:

$$\langle F_A \rangle = \langle \rho v_\perp^2 (v_A + v_r) + p_A v_r \rangle = \left\langle -\frac{B_r B_\perp v_\perp}{4\pi} \right\rangle + \left\langle \left(\frac{\rho v_\perp^2}{2} + \frac{B_\perp^2}{8\pi} \right) v_r \right\rangle + \left\langle \frac{B_\perp^2}{8\pi} v_r \right\rangle, \quad (9)$$

where we define Alfvén wave pressure as $p_A = B_\perp^2 / 8\pi$. In the upper panel of Figure 3 we plot the wave energy flux, $\langle F_A \rangle \frac{r^2 f(r)}{r_c^2 f(r_c)}$, normalized by cross section of the flux tube at $r_c = 1.02 R_\odot$ with kinetic energy flux, $\rho v_r \frac{v_r^2}{2} \frac{r^2 f(r)}{r_c^2 f(r_c)}$, enthalpy flux, $\rho v_r (e + \frac{p}{\rho}) \frac{r^2 f(r)}{r_c^2 f(r_c)}$, and integrated radiative loss, $\int_{R_\odot}^r q_R \frac{r^2 f(r)}{r_c^2 f(r_c)} dr$. Note that the real energy flux is larger (smaller) in $r < r_c$ ($r > r_c$). While the most of the initial wave energy escapes by radiation loss in the chromosphere and the low corona, the remained energy, which is $\sim 10\%$ of the input, is transferred to the kinetic energy of the solar wind in the outer region. The thermal energy is almost constant in the corona, which indicates that the ~ 1 MK plasma is maintained by the energy balance among wave heating, radiative cooling, adiabatic cooling (solar wind acceleration), and redistribution by thermal conduction.

The lower panel of Figure 3 plots measure of pressure of Alfvén waves, $\langle p_A v_r \rangle$, and thermal gas, $\langle p v_r \rangle$. This shows that the Alfvén wave pressure dominates the gas pressure in the solar wind acceleration region ($1.5 R_\odot \lesssim r \lesssim 10 R_\odot$); the fast solar wind is driven by the wave pressure rather than by the thermal pressure.

In paper I, we claimed that the dissipation of the low-frequency Alfvén waves in the corona is mainly by the generation of slow waves and reflection of the Alfvén waves due to the density fluctuation of the slow modes. This can be seen in $r - t$ diagrams. Figure 4 presents contours of amplitude of v_r , ρ , v_\perp , and B_\perp / B_r in $R_\odot \leq r \leq 15 R_\odot$ from $t = 2570$ min. to 2600 min. Dark (light) shaded regions denote positive (negative) amplitude. Above the panels, we indicate the directions of the local 5 characteristics, two Alfvén, two slow, and one entropy waves at the respective positions. Note that the fast MHD and Alfvén modes degenerate in our case (wave vector and underlying magnetic field are in the same direction), so we simply call the innermost and outermost waves Alfvén modes. In our simple 1D geometry, v_r and ρ trace the slow modes which have longitudinal wave components, while v_\perp and B_\perp trace the Alfvén modes which are transverse (see Cho & Lazarian [2002;2003] for more general cases.).

One can clearly see the Alfvén waves in v_\perp and B_\perp / B_r diagrams, which have the same slopes with the Alfvén characteristics shown above. One can also find the incoming modes propagating from lower-right to upper-left as well as the outgoing modes generated from the surface¹. These incoming waves are generated by the reflection at the ‘density mirrors’ of the slow modes (see paper I).

At intersection points of the outgoing and incoming characteristics the non-linear wave-wave interactions take place, which play a role in the wave dissipation.

The slow modes are seen in v_r and ρ diagrams. Although it might be difficult to distinguish, the most of the patterns are due to the outgoing slow modes² which are generated from the perturbations of the Alfvén wave pressure, $B_{\perp}^2/8\pi$ [Kudoh & Shibata, 1999; Tsurutani et al., 2002]. These slow waves steepen eventually and lead to the shock dissipation.

The processes discussed here are the combination of the direct mode conversion to the compressive waves and the parametric decay instability due to three-wave (outgoing Alfvén, incoming Alfvén, and outgoing slow waves) interactions (Goldstein 1978; Terasawa et al. 1986; see also §4.1.2) of the Alfvén waves. Although they are not generally efficient in the homogeneous background since they are the nonlinear mechanisms, the density gradient of the background plasma totally changes the situation. Owing to the gravity, the density rapidly decreases in the corona as r increases, which results in the amplification of the wave amplitude so that the waves easily become nonlinear. Furthermore, the Alfvén speed varies a lot due to the change of the density even within one wavelength of Alfvén waves with periods of minutes or longer. This leads to both variation of the wave pressure in one wavelength and partial reflection through the deformation of the wave shape [Moore et al., 1991]. The dissipation is greatly enhanced by the density stratification, in comparison with the case of the homogeneous background. Thus, the low-frequency Alfvén waves are effectively dissipated, which results in the heating and acceleration of the coronal plasma.

In summary, we have shown that the low-frequency Alfvén waves are dissipated via the combination of the direct mode conversion and the decay instability which are considerably enhanced by the long wavelength (so called “non-WKB”) effect in the stratified atmosphere. Although each process is not individually effective enough, the significant dissipation rate is realized by the combination.

4. Universality and Diversity

We investigate how the properties of the corona and solar wind depend on the parameters of the input photospheric fluctuations and the flux tube geometry. We use smaller simulation boxes in Run II-IX than in Run I (Table 1) to save the computational time for the parameter studies. In most cases quasi-steady state conditions are achieved after $t \gtrsim 30$ hr. In this section we show results at $t = 48.3$ hr unless explicitly stated.

4.1. Various Input Waves

4.1.1. Wave Spectrum

We show dependences on the spectrum, $P(\nu)$, of the photospheric fluctuations. We here compare the results of $P(\nu) \propto \nu^{-1}$ ($6 \times 10^{-4} < \nu < 2.5 \times 10^{-2}$ Hz; Run II), ν^0 (white noise; Run III), and purely sinusoidal perturbation with a period of 180 s, $P(\nu) \propto \delta(\nu^{-1} - 180\text{s})$ (Run IV). Figure 5 shows structure of the coronae and solar winds. The upper panel of Figure 6 plots an adiabatic constant, S_c , of the outgoing Alfvén wave derived from wave action [Jacques, 1977]:

$$S_c = \rho \langle \delta v_{A,+}^2 \rangle \frac{(v_r + v_A)^2}{v_A} \frac{r^2 f(r)}{r_c^2 f(r_c)}, \quad (10)$$

where

$$\delta v_{A,+} = \frac{1}{2} \left(v_{\perp} - B_{\perp} / \sqrt{4\pi\rho} \right) \quad (11)$$

is amplitude of the outgoing Alfvén wave (Elsässer variables). The lower panel shows nonlinearity, $\langle \delta v_{A,+} \rangle / v_A$ of the outgoing Alfvén waves.

Figure 5 shows that the plasma is heated up to the coronal temperature and accelerated to 400-600km/s at 0.1AU in all the Runs. Particularly, the results of $P(\nu) = \nu^{-1}$ and ν^0 are quite similar. The attenuation of the outgoing Alfvén waves is due to the two kinds of the processes, the shocks and the reflection in our simulations. The shock dissipation per unit distance is larger for waves with larger ν because the number of shocks is proportional to wavenumber. On the other hand, Alfvén waves with smaller ν suffer the reflection more since the wavelengths are relatively larger compared to the variation scale of the Alfvén speed so that the wave shapes are deformed more. These two ingredients with respect to the ν -dependence cancel in these two cases, and the variations of the energy and the amplitude become quite similar (Figure 6). The structures of the corona and the solar wind are also similar since they are consequences of the wave dissipation.

The results of the purely sinusoidal fluctuation (Run IV) are slightly different from the other two cases. The TR is not so sharp as those in the other two Runs. The temperature firstly rises at $r - R_{\odot} = 0.005R_{\odot}$, but drops slightly and again rises around $r - R_{\odot} = 0.02R_{\odot}$. Actually, the TR moves back and forth more compared to the other cases. This is because the shock heating takes place rather intermittently only at the wave crests of the monochromatic wave, while in the other cases the heating is distributed more uniformly by the contributions from waves with various ν 's. As a result, the chromospheric evaporation occurs intermittently so that the TR becomes “dynamical”. The sharpness of the TR is important in terms of the wave reflection. In the sinusoidal case (Run IV) the Alfvén waves become more transparent at the TR since the variation of the Alfvén speed is more gradual. Therefore, more wave energy transmits into the corona, avoiding the reflection at the TR (Figure 6). Accordingly, the temperature and density in the outer region become higher owing to the larger plasma heating (Figure 5).

4.1.2. Wave Polarization

We examine the effect of the wave polarization. Linearly polarized Alfvén waves dissipate by the direct steepening [Hollweg, 1982; Suzuki, 2004] to MHD fast shocks as well as by the parametric decay instability [Goldstein, 1978]. On the other hand, circularly polarized components do not steepen, and it dissipates only by the parametric decay instability in our one-fluid MHD framework, so that the dissipation becomes less efficient.

Figures 7 and 8 compare the results of sinusoidal linearly polarized (Run IV) and circularly polarized (Run V) fluctuations with the same amplitude ($\langle (dv_{\perp}, 0) \rangle = 0.7\text{km s}^{-1}$). The results of Run II are also plotted for comparison. It is shown that the coronal heating and solar wind acceleration are still achieved by the dissipation of the circularly polarized Alfvén waves (Figure 7) although a large fraction of the wave energy remains at the outer boundary (Figure 8) owing to the less dissipative character as expected.

A key ingredient for the efficient dissipation is the rapid decrease of the density owing to the gravity as discussed in §3. The circularly polarized Alfvén waves which are initially sinusoidal are quickly deformed by the rapid variation of the density in the chromosphere and the low corona; simple sinusoidal waves cannot propagate any further unless the wavelengths are sufficiently short. The shape deformation indicates that the waves are partially reflected and the incoming Alfvén waves are generated. Compressive slow waves are also easily generated even without the steepening because the variation of the magnetic pressure is present owing to the large difference of the Alfvén speed within one wavelength [Boynton & Torkelsson, 1996; Ofman & Davila, 1997, 1998; Grappin et al., 2002].

It has been generally believed that the decay instability of the Alfvén waves is not important in the context of the coronal heating and the solar wind acceleration. However, our simulation shows that this is not the case; the three-wave interactions are greatly enhanced by the long wavelength effect so that the sufficient wave dissipation occurs in the real solar corona.

The case of the circularly polarized waves gives smaller coronal density and temperature since the wave dissipation is less effective. However, the solar wind speed is rather faster, up to 700km s⁻¹ at

0.1AU, because the less dense plasma can be efficiently accelerated by transfer from the momentum flux of the Alfvén waves.

4.1.1.3. Wave Amplitude

We study dependences on the amplitudes of the input fluctuations at the photosphere. We compare the results of larger $\langle dv_{\perp,0} \rangle = 1.4 \text{ km s}^{-1}$ (Run VI) and smaller $\langle dv_{\perp,0} \rangle = 0.4 \text{ km s}^{-1}$ (Run VII) cases with the fiducial case ($\langle dv_{\perp,0} \rangle = 0.7 \text{ km s}^{-1}$; Run II) in Figures 9 and 10. We also show the results of $\langle dv_{\perp,0} \rangle = 0.3 \text{ km s}^{-1}$ (Run IX) at $t = 18.3 \text{ hr}$ in Figure 9, although quasi steady-state behavior is not achieved. At later time in Run IX, the density and temperature decrease with time as explained later.

The maximum temperature of Run VII ($\langle dv_{\perp,0} \rangle = 0.4 \text{ km s}^{-1}$) is $\simeq 5 \times 10^5 \text{ K}$, which is cooler than the usual corona. The density is much lower than the fiducial case by 1-2 orders of magnitude because the sufficient mass cannot supply into the corona by the chromospheric evaporation owing to the low temperature; the evaporation is drastically suppressed as T decreases since the conductive flux ($F_c \propto T^{5/2} \frac{dT}{dr}$) sensitively depends on T . As a result, the mass flux (ρv_r) becomes more than an order of magnitude lower than that of the present solar wind. These tendencies are more extreme in Run IX; The coronal temperature and density become further low in Run IX; $T \simeq 2 \times 10^5 \text{ K}$ and the density in the corona and solar wind is smaller by 3 orders of magnitude than the fiducial case.

This behavior can be understood by the wave dissipation (Figure 10). The input wave energy ($\propto \langle dv_{\perp,0}^2 \rangle$) in Run VII is 1/3 of that of Run II. However, the upper panel of Figure 10 shows that the remained S_c 's in both cases are similar at 0.1AU, which indicates that the Alfvén waves do not effectively dissipate in the smaller $\langle dv_{\perp,0} \rangle$ case. This is because the Alfvén speed ($= B/\sqrt{4\pi\rho}$) is larger due to the lower density and the nonlinearity, $\langle \delta v_{A,+} \rangle / v_A$, becomes weaker. As a result, the final energy flux of the solar wind at 0.1AU, mostly consisting of the kinetic energy ($\rho v_r \frac{v_r^2}{2}$), becomes one order of magnitude smaller although the ratio of the input wave energy is only 1/3.

Once the coronal density starts to decrease, a positive feedback operates. Namely, the decrease of the density leads to weaker non-linearity of the Alfvén waves, which reduces the plasma heating by the wave dissipation. This decreases the coronal temperature, and further reduces the coronal density by the suppression of the chromospheric evaporation. This takes place in Run IX ($\langle dv_{\perp,0} \rangle = 0.3 \text{ km s}^{-1}$) so that the coronal density and temperature continue to decrease at later time, instead of maintaining steady corona and solar wind.

Our results show that $\langle dv_{\perp,0} \rangle \gtrsim 0.4 \text{ km s}^{-1}$ is the criterion of the photospheric fluctuations for the formation of the stable hot plasma. To get the maximum coronal temperature $\gtrsim 10^6 \text{ K}$, $\langle dv_{\perp,0} \rangle \gtrsim 0.7 \text{ km s}^{-1}$ is required. Otherwise if $\langle dv_{\perp,0} \rangle \lesssim 0.3 \text{ km s}^{-1}$, the low-frequency Alfvén waves cannot maintain the hot corona, and the solar wind mass flux becomes drastically small; solar winds *virtually disappear* (see §4.1.4).

The solar wind speeds are slightly faster in the cases of smaller $\langle dv_{\perp,0} \rangle$ (accordingly smaller energy input), because the densities at the coronal bases are much smaller owing to the suppression of the chromospheric evaporation; the smaller amounts of the materials are accelerated to the faster speeds. The differences between the photospheric and coronal base densities are larger in the smaller $\langle dv_{\perp,0} \rangle$ cases and the amplification of dv_{\perp} ($\propto \rho^{-1/4}$ if Alfvén waves are nondissipative in static media; e.g. Lamers & Cassinelli 1999) is larger. As a result, $\langle dv_{\perp} \rangle$ at the coronal base is (weakly) anti-correlated with $\langle dv_{\perp,0} \rangle$ at the photosphere. Thus, our result is consistent with the previous calculations [Sandbæk & Leer, 1995; Ofman & Davila, 1998] that show the positively correlation between the Alfvén wave amplitude at the coronal base and the solar wind speed.

Larger $\langle dv_{\perp,0} \rangle$ gives larger coronal density as shown in Run VI. The initial increase of the temperature starts from a deeper location around $r \simeq 0.005 R_{\odot}$ than the other cases. Thanks to this, a decrease of the density is slower (larger pressure scale height) so that the density around $r = 1.01 R_{\odot}$ is two orders of magnitude larger than that of Run II. However, the temperature decreases

slightly instead of a monotonical increase; it cannot go over the peak of the radiative cooling function at $T \simeq 10^5 \text{ K}$ [Landini & Monsignori-Fossi, 1990] because the radiative loss is efficient owing to the large density. The second increase of the temperature begins from $r \simeq 1.03 R_{\odot}$ and above there the corona is formed. The coronal density and temperature are larger than those in Run II. In particular the density in the outer region is 10 times larger, and the mass flux of the solar wind is larger by the same extent. The top panel of Figure 10 shows that the Alfvén waves dissipate more effectively in the larger $\langle dv_{\perp,0} \rangle$ case by the same mechanism as explained above for the smaller $\langle dv_{\perp,0} \rangle$ cases.

Figure 11 summarizes the maximum coronal temperature, $T_{\text{max}}(\text{K})$ (top), the solar wind mass flux at 0.1AU, $(\rho v_r)_{0.1\text{AU}}(\text{g cm}^{-2} \text{ s}^{-1})$ (middle), and solar wind speed at 0.1AU, $v_{r,0.1\text{AU}}(\text{km s}^{-1})$, (bottom) as functions of $\langle dv_{\perp,0} \rangle(\text{km s}^{-1})$. On the right axis of the middle panel, we show the proton flux at 1AU, $(n_p v_r)_{1\text{AU}}(\text{cm}^{-2} \text{ s}^{-1})$. When deriving $(n_p v_r)_{1\text{AU}}$ from $(\rho v_r)_{0.1\text{AU}}$, we use the relation of $\rho v_r \propto r^{-2}$, and assume the solar elemental abundance. T_{max} and $(\rho v_r)_{0.1\text{AU}}$ have positive correlations with $\langle dv_{\perp,0} \rangle$. The dependence of $(\rho v_r)_{0.1\text{AU}}$ is quite steep because of the nonlinearity of the Alfvén waves as explained above. The dependence of T_{max} is more gradual due to the redistribution of the temperature by the thermal conduction. $v_{r,0.1\text{AU}}$ has weakly negative correlation with $\langle dv_{\perp,0} \rangle$ for $\langle dv_{\perp,0} \rangle \geq 0.4(\text{km s}^{-1})$ because in smaller $\langle dv_{\perp,0} \rangle$ cases the coronal density is further lower and smaller amounts of materials are accelerated more effectively. For $\langle dv_{\perp} \rangle = 0.3(\text{km s}^{-1})$, the coronal temperature and the mass flux of the solar wind becomes smaller later time and the wind speed varies quite a lot; we use upper limits for T_{max} and $(\rho v_r)_{0.1\text{AU}}$, and a dashed error bar for $v_{r,0.1\text{AU}}$.

In our simulation we only consider the steady fluctuations with constant $\langle dv_{\perp,0} \rangle$'s to study the basic relation between the footprint fluctuations and the properties of the solar winds. In the real situation, however, $\langle dv_{\perp,0} \rangle$ would vary in time. Our results imply that a small temporal variation of $\langle dv_{\perp,0} \rangle$ at the surface possibly leads to large time dependent behavior of the solar wind. As one example we would like to discuss an event of solar wind disappearance in the following section.

4.1.1.4. Disappearance of Solar Wind

On May 10-12, 1999, observed solar wind density near the earth drastically decreases well below 1 cm^{-3} for \sim a day and to 0.1 cm^{-3} at the lowest level, in comparison with the typical value $\sim 5 \text{ cm}^{-3}$ [Le et al., 2000; Smith et al., 2001]. Various mechanisms are widely discussed to explain this disappearance event [Usmanov et al., 2000; Richardson et al., 2000; Crooker et al., 2000]. In §4.1.3, we have shown that the solar wind density sensitively depends on the amplitude of the photospheric fluctuation provided that the non-linear dissipation of low-frequency Alfvén waves operates in the solar wind heating and acceleration. According to Figure 11 the solar wind density and mass flux becomes ~ 100 and ~ 50 times smaller respectively if $\langle dv_{\perp,0} \rangle$ changes from 0.7 km s^{-1} to 0.4 km s^{-1} ; a small variance of the energy injection at the solar surface leads to a large variation of the solar wind density because of the nonlinearity. Therefore, we can infer that if the amplitude of the photospheric turbulence becomes $\sim 1/2$ during \sim a day, this event of the solar wind disappearance is possibly realized.

The observation shows that the velocity of the sparse plasma discussed above is lower than that of the surrounding plasma, which is inconsistent with our results (§4.1.3). We are speculating that the stream interaction would resolve the inconsistency. The sparse region is easily blocked by the preceding dense plasma in the spiral magnetic fields (Parker spiral) even if its speed in the inner region (say $\sim 0.1\text{AU}$) is faster [Usmanov et al., 2000], because the ram pressure is much smaller than that of the surrounding plasma. For quantitative arguments, however, two dimensional modeling is required.

4.2. Flux Tube properties

It is widely believed that field strength and geometry of open flux tubes are important parameters that control the solar wind speed. Wang & Sheeley [1990, 1991] showed that the solar wind speed at ~ 1 AU is anti-correlated with f_{\max} from their long-term observations as well as by a simple theoretical model. Ofman & Davila [1998] showed this tendency by time-dependent simulations as well. Fisk et al. [1999] claimed that the wind speed should be positively correlated with $B_{r,0}$ by a simple energetics consideration. Kojima et al. [2005] have found that the solar wind velocity is better correlated with the combination of these two parameters, $B_{r,0}/f_{\max}$, than $1/f_{\max}$ or $B_{r,0}$ from the comparison of the outflow speed obtained by their interplanetary scintillation measurements with observed photospheric field strength. Suzuki [2004] and Suzuki [2006] also pointed out that $B_{r,0}/f_{\max}$ should be the best control parameter provided that the Alfvén waves play a dominant role in the coronal heating and the solar wind acceleration.

Here we test the last scenario by our simulation. In Figures 12 and 13, we compare the results of a flux tube with smaller $B_{r,0}/f_{\max} = 322(\text{G})/450$ (Run VIII) with the fiducial case ($B_{r,0}/f_{\max} = 161(\text{G})/75$) (Run II) for the polar coronal hole. We chose the parameters of Run VIII with equatorial and mid-latitude coronal holes in mind; they are surrounded by closed structures, and thus, have moderately larger photospheric field strength and much larger flux tube divergence than the polar coronal hole.

Figure 12 shows that Run VIII gives much slower solar wind speed which is consistent with Kojima et al. [2005], Suzuki [2004], and Suzuki [2006], with slightly hotter and denser corona. These results can be understood by positions of the wave dissipation. The upper panel of Figure 13 indicates that the outgoing Alfvén waves dissipate more rapidly in the smaller $B_{r,0}/f_{\max}$ case. This is because the nonlinearity of the Alfvén waves, $\langle \delta v_{A,+} \rangle / v_A$ is larger due to smaller $v_A \propto B_r$ ($\propto B_{r,0}/f_{\max}$ in the outer region where the flux tube is already super-radially open) even though the absolute amplitude ($\langle dv_{\perp} \rangle$) is smaller (bottom panel of Figure 12). As a result, more wave energy dissipate in the smaller $B_{r,0}/f_{\max}$ case in the subsonic region and less energy remains in the supersonic region. In general, energy and momentum inputs in the supersonic region gives higher wind speed, while those in the subsonic region raises the mass flux (ρv_r) of the wind by an increase of the density [Lamers & Cassinelli, 1999]. Therefore, the smaller $B_{r,0}/f_{\max}$ case gives slower wind with higher coronal density, whereas the solar wind density in the outer region is similar to that of the larger $B_{r,0}/f_{\max}$ case on account of the dilution of the plasma in the more rapidly expanding flux tube. We can conclude that $B_{r,0}/f_{\max}$ controls the solar wind speed and the coronal density through the nonlinear dissipation of the Alfvén waves.

4.3. Summary of Parameter Studies

We have examined the dependences of the coronal and wind properties on the various wave and flux tube parameters in §4.1 and §4.2. One of the important results is that we do not find any subsonic ‘breeze’ solution in our simulations. All the Runs with $\langle dv_{\perp,0} \rangle \gtrsim 0.3 \text{ km s}^{-1}$ show the transonic feature, hence, transonic solar winds are natural consequences of the dissipation of the low-frequency Alfvén waves. Smaller energy injection only reduces the density (and consequently the mass flux) of the wind. The wind speed itself is rather slightly faster for smaller wave energy because the coronal base density becomes lower owing to the suppression of the chromospheric evaporation.

From §4.1.1 and §4.1.2, we can conclude that the dependences on the spectra and polarizations of the input fluctuations are weak as long as the low-frequency ($\lesssim 0.05 \text{ Hz}$) waves are considered. $\langle dv_{\perp,0} \rangle$ and $B_{r,0}/f_{\max}$ are the important control parameters, and the dependences are summarized below:

- The coronal temperature and the density in the corona and solar wind are mainly determined by the photospheric amplitude, $\langle dv_{\perp,0} \rangle$. The corona with temperature $\gtrsim 10^6 \text{ K}$ is formed if $\langle dv_{\perp,0} \rangle \gtrsim 0.7 \text{ km s}^{-1}$. Larger $\langle dv_{\perp,0} \rangle$ gives higher density in the corona and the solar wind. If $\langle dv_{\perp,0} \rangle \lesssim 0.3 \text{ km s}^{-1}$ the hot plasma cannot be maintained and the mass flux of the solar wind is unrealistically small.
- The solar wind speed is mainly controlled by $B_{r,0}/f_{\max}$; faster winds come from open flux tubes with larger $B_{r,0}/f_{\max}$.

5. Fast and Slow Solar Winds

The observed solar winds can be categorized into two distinctive types. One is the fast solar wind which is mainly from polar coronal holes and the other is the slow wind which is from mid- to low-latitude regions. Apart from the velocity difference, both density of solar winds [Phillips et al., 1995] and freezing-in temperatures of heavy ions [Geiss et al., 1995] which reflect the coronal temperatures are anti-correlated with velocities. Origins of the slow solar wind are still in debate; there are mainly two types argued (see Wang et al. 2000 for review). One is the acceleration due to intermittent break-ups of the cusp-shaped closed fields in the equatorial region (e.g. Endeve, Leer, & Holtzer 2003). The other is the acceleration in open flux tubes with large areal expansions in low- and mid-latitude regions. Kojima et al. [1999] detected low-speed winds with single magnetic polarities, originating from open structure regions located near active regions, which indicates a certain fraction of the slow stream is coming from open regions, similarly to the fast wind. In this paper we focus on the latter case with respect to the slow solar wind.

Based on our parameter studies summarized in §4.3, we can infer the suitable $\langle dv_{\perp,0} \rangle$ and $B_{r,0}/f_{\max}$ for the slow solar wind by comparing with those for the fast wind (Run I/II; also in paper I); the slow wind requires larger $\langle dv_{\perp,0} \rangle$ and smaller $B_{r,0}/f_{\max}$ than the fast wind. The adopted parameters are summarized in table 1 (Run X).

In the panels on the left side of Figure 14 we compare the results of Run X (slow wind) and Run I (fast wind) overlaid with recent observations of slow solar winds (see Figure 2 for the observations of fast winds). The temperature and density of the slow wind case becomes larger on account of the larger $\langle dv_{\perp,0} \rangle$, which explains the observations. On the other hand, smaller $B_{r,0}/f_{\max}$ gives slower terminal speed. As a result, the observed anti-correlation of the wind speed and the coronal temperature [Schwadron & McComas, 2003] is well-explained by our simulations. In the slow wind case (Run X), the acceleration of the outflow is more gradual, and it is not negligible in $r \gtrsim 20 R_{\odot}$ (e.g. Nakagawa et al. 2005).

In the panels on the right of Figure 14, we show the properties of the wave dissipation. The top right panel compares transverse amplitude, $\langle dv_{\perp} \rangle$, averaged over 28 minutes in the fast and slow wind cases. $\langle dv_{\perp} \rangle$ is larger in the fast wind. This is because the Alfvén waves become less dissipative in the fast wind conditions; larger B ($\propto B_0/f_{\max}$) and smaller ρ give larger v_A so that the nonlinearity of the Alfvén waves, $\langle \delta v_{A,+} \rangle / v_A$, is systematically smaller. As a result, the Alfvén wave dissipates more slowly in the fast wind case, which is shown in the plot of S_c of the wave (the bottom right panel of Figure 14). This tendency of the larger $\langle dv_{\perp} \rangle$ in the fast wind is expected to continue to the outer region, $\gtrsim 1$ AU. Various in situ observations in the solar wind plasma near the earth also show that the fast wind contains more Alfvénic wave components (see Tsurutani & Ho 1999 for review), which can be explained via the nonlinear dissipation of Alfvén waves based on our simulations.

The middle right panel of Figure 14 shows longitudinal fluctuation, $\langle dv_{\parallel} \rangle$, averaged over 28 minutes. $\langle dv_{\parallel} \rangle$ reflects the amplitude of slow MHD waves generated from the Alfvén waves via the nonlinear process (§3). Slow waves are identified in polar regions [Ofman et al., 1999] and low-latitude regions [Sakurai et al., 2002] at low altitudes ($r \lesssim 1.2 R_{\odot}$). The observed amplitudes are still small ($\simeq 7.5 \text{ km s}^{-1}$ in the polar regions and $\simeq 0.3 \text{ km s}^{-1}$ in the low-latitude regions) because of the large density there, which is consistent with our results. What is more interesting is longitudinal fluctuations in outer regions. our results exhibits that

$\langle dv_{\parallel} \rangle$ in the solar wind plasma is not small. Typically, the simulations give $\langle dv_{\parallel} \rangle \sim 100\text{km/s}$ in $3R_{\odot} \lesssim r \lesssim 10R_{\odot}$ of the fast wind and $\langle dv_{\parallel} \rangle \sim 20\text{km/s}$ in $2R_{\odot} \lesssim r \lesssim 10R_{\odot}$ of the slow wind, whereas these might be modified if we take into account multi-dimensional effects (§6.2). This is directly testable by in situ measurements of future missions, Solar Orbiter and Solar Probe, which will approach to ~ 45 and $4R_{\odot}$, respectively, corresponding to the inside of our computation domain.

Our simulations show that the different types of the solar winds can be explained by the single process, the dissipation of the low-frequency Alfvén waves, although we do not intend to exclude other possibilities. The varieties of the solar winds are due to the varieties of the footpoint amplitudes as well as the magnetic fields and geometry of the flux tubes. Our choice of $B_{r,0}/f_{\text{max}}$ is consistent with the obtained data by Kojima et al. [2005] who report that the slow winds are mainly from the low-to mid-latitude coronal holes with smaller $B_{r,0}/f_{\text{max}}$. In contrast, quantitative arguments on $\langle dv_{\perp,0} \rangle$ need more detailed fine scale observations of the magnetic fields with high cadence by future telescopes such as Solar-B.

6. Discussions

6.1. Wave Generation

In this paper we have assumed that the origin of the waves is the steady turbulent motions at the photosphere. However, transient activities are also expected to play a role in the wave generation. Sturrock [1999] proposed small flare-like events triggered by magnetic reconnections of closed loops in the chromosphere excite MHD waves in the corona. Miyagoshi et al. [2005] also show that interactions between open field lines and emergent flux tubes excite Alfvén waves at a location above the photosphere. These waves could directly heat up the corona since they do not suffer the attenuation in the chromosphere and the TR.

An important issue for the wave generation by these transient events is the energetics. The energy release from each event is generally thought to be small, categorized as a micro- or nano-flare [Parnell & Jupp, 2000; Katsukawa & Tsuneta, 2001]. To clarify how these waves dominantly work in the heating and acceleration of the solar wind, we should determine the frequency of these events. These small-scale events might be important in the heating of not only the open coronal holes but the closed regions. The determination of the total energy release from small transient events by future observations is quite important in terms of the coronal heating in various portions of the corona.

6.2. Limitation of Our Simulations

We have shown by the self-consistent simulations that the dissipation of the low-frequency Alfvén waves through the generation of the compressive waves and shocks is one of the solutions for the heating and acceleration of the plasma in the coronal holes. However, the validity of the 1D MHD approximation needs to be examined.

We think that the MHD approximation is appropriate as a whole for studies of the average properties of the plasma. Let us estimate the Larmor radius, l_{Larmor} , of the protons which compose the main part of the plasma due to fluctuations of field lines, B_{\perp} , under the coronal condition. Typically, $B_{\perp} \sim 0.1B_r \sim 0.1\text{G}$, and then $l_{\text{Larmor}} \sim 0.1\text{km}$ for a thermal proton with $\sim 100\text{km s}^{-1}$. On the other hand the shortest wavelength, λ_{min} , of the Alfvén waves we are considering is $\lambda_{\text{min}} \sim 3 \times 10^4\text{km}$ (a period of 20s and $v_A \sim 1500\text{km s}^{-1}$.) and the simulation grid size in the corona is $\sim 3 \times 10^3\text{km}$ ($\sim 1/10$ of λ_{min}); the thermal protons are supposed to be well randomized through turbulent magnetic fields on the scales we are dealing with.

In our simulations the heating of the plasma is done by MHD shocks (§2). Our simulations cannot resolve detailed structures of shocks since the size of the grid is larger than the width of the shock front which is an order of a Larmor radius. However,

the global structure of shocks can be appropriately treated by our simulations. The thermal particles could be ‘trapped’ around the shock regions by the random magnetic fields so that the global properties of shocks would satisfy the MHD condition. Therefore, the shock heating rate calculated in our MHD simulations is supposed to give a reasonable estimate in the coronal region. In the outer region ($r \gtrsim 2R_{\odot}$), $l_{\text{Larmor}} (\propto 1/B)$ increases and $\lambda_{\text{min}} (\sim v_A/\nu_{\text{max}} \propto v_A \propto B/\sqrt{\rho})$ decreases as r increases. Even around 0.3AU , l_{Larmor} is about $\sim 1/10$ of λ_{min} ; the approximation still remains reasonable.

However, we should be cautious about the fact that the shocks are collisionless; mean free path due to Coulomb collisions, which is $\sim 100\text{km}$ for electron-electron collisions and even larger for electron-proton and proton-proton collisions under the typical coronal condition ($T = 10^6\text{K}$ and $n = 10^9\text{cm}^{-3}$), is much larger than l_{Larmor} so that the particles are not thermalized by Coulomb collisions but only randomized by fluctuating fields. In such a condition, the particle distribution function possibly deviates from the Maxwell-Boltzmann distribution, which is actually observed in solar wind plasma [Marsch et al., 1982a]. Non-thermal, or even supra-thermal, particles might modify the heating rate, if their amount is not negligible. The shock energy is transferred not only to the thermal heating but also to acceleration of the nonthermal component. Although this is beyond the scope of the present paper, this issue should be carefully considered in more detailed models.

Effects of multi-component plasma also need to be taken into account [Lie-Svendsen, 2001; Ofman, 2004]. The thermal conduction and radiative cooling are mainly involved with electrons, and the electron temperature becomes systematically lower than the ion temperature without effective thermal coupling by Coulomb collisions. The observed proton temperature is actually higher than the electron temperature even around a few solar radii [Esser et al., 1999]. The temperature in our simulations represents the electron temperature because it is mainly determined by the thermal conduction and radiative cooling. The actual thermal pressure is supposed to be higher than the simulated temperature due to the higher proton temperature. Therefore, the acceleration profile might be slightly modified whereas the dynamics are mostly controlled by the magnetic pressure of the Alfvén waves.

Collisionless processes would also be important for the wave dissipation [Tsurutani et al., 2005]. The heating rates by the dissipation of Alfvén waves are different for electrons and ions [Hasegawa & Lui, 1975; Tsiklauri et al., 2005]. The compressive waves generated from the Alfvén waves would suffer transit-time damping by interactions between magnetic mirrors and surfing particles [Barnes, 1966; Suzuki, 2006]. If high-frequency (ion-cyclotron) waves are produced by frequency cascade, the heating sensitively depends on mass-to-charge ratios of particles [Dusenberry & Hollweg, 1981; Marsch et al., 1982b]. It is believed that this process can explain the observed preferential heating of the perpendicular temperature of the heavy ions [Kohl et al., 1998], while there are potential difficulties in the proton heating as discussed in §1.

In the chromosphere, the gas is not fully ionized. In such circumstances, the friction due to ion-neutral collisions might be important in the dissipation of Alfvén waves [Lazarian et al., 2004; Yan & Lazarian, 2004].

Generally, the shock dissipation tends to be overestimated in 1D simulations because the waves cannot be diluted by the geometrical expansion. On the other hand, there are other mechanisms of the wave damping due to the multi-dimensionality [Ofman, 2004], such as phase mixing [Heyvaerts & Priest, 1983; Nakariakov et al., 1998; De Moortel et al., 2000] and refraction [Bogdan et al., 2003]. Moreover, the solar wind plasma is more or less turbulent and it must be important to take into account the plasma heating through cascades of Alfvénic turbulences in the transverse direction [Goldreich & Sridhar, 1995; Mattheus et al., 1999; Oughton et al., 2001]. Studies of the imbalanced cascade, in which a wave component in one direction has larger energy than that in the counter direction, seem to be important for us to understand transport phenomena in the solar wind plasma [Lithwick & Goldreich, 2003], though it has not been fully understood yet.

Therefore, the Alfvén waves might also be dissipated by mechanisms different from those included in our simulations. Accordingly, variation of wave amplitudes might be modified when these additional dissipation processes are considered. Self-consistent simulations including these various processes remain to be done in order to arrive at final conclusion.

7. Summary

We have performed parametric studies of the coronal heating and solar wind acceleration by the low-frequency Alfvén waves in open coronal holes. We have performed 1D MHD numerical simulations from the photosphere to 0.3 or 0.1AU. The low-frequency Alfvén waves with various spectra, polarization, and amplitude are generated by the footpoint fluctuations of the magnetic field lines. We have treated the wave propagation and dissipation, and the heating and acceleration of the plasma in a self-consistent manner.

We have found that the transonic solar winds are accomplished in all the simulation Runs. Smaller energy injection does not reduce the outflow speed but the density to maintain the transonic feature. The atmosphere is heated up to the coronal temperature ($\gtrsim 10^6$ K) if the photospheric amplitude, $\langle dv_{\perp,0} \rangle \gtrsim 0.7\text{km s}^{-1}$. Otherwise, the temperature and density become much lower than the present coronal values. If $\langle dv_{\perp,0} \rangle \lesssim 0.3\text{km s}^{-1}$, the temperature becomes less than a few 10^5 K and the sufficient mass cannot be supplied into the corona owing to the suppression of the chromospheric evaporation. The stable hot corona cannot be maintained any longer, and the mass flux of the solar wind becomes at least 3 orders of magnitude smaller than the observed value of the present solar wind. This shows that the solar wind almost disappears only by reducing the photospheric fluctuation amplitude by half. On the other hand, the case with $\langle dv_{\perp,0} \rangle = 1.4\text{km s}^{-1}$ gives 10 times larger density than the fiducial case ($\langle dv_{\perp,0} \rangle = 0.7\text{km s}^{-1}$). These sensitive behaviors of the solar wind mass flux on $\langle dv_{\perp,0} \rangle$ can be explained via the nonlinear dissipation of Alfvén waves. Our simulations have also confirmed that the positive correlation of the solar wind speed with $B_{r,0}/f_{\text{max}}$ obtained by Kojima et al. [2005].

We have finally pointed out that both fast and slow solar winds can be explained even solely by the dissipation of the low-frequency Alfvén waves with different $\langle dv_{\perp,0} \rangle$ and $B_{r,0}/f_{\text{max}}$, whereas we do not intend to exclude other possibilities. Fast winds are from flux tubes with larger $B_{r,0}/f_{\text{max}}$ and smaller $\langle dv_{\perp,0} \rangle$, while slow winds are from flux tubes with smaller $B_{r,0}/f_{\text{max}}$ and larger $\langle dv_{\perp,0} \rangle$. These choices naturally explain the following observed tendencies: (i) the anti-correlation of the solar wind speed and the coronal temperature, and (ii) the larger amplitude of Alfvén waves in the fast wind in the interplanetary space. The tendency with respect to $B_{r,0}/f_{\text{max}}$ is consistent with the observed trend [Kojima et al., 2005]. To determine $\langle dv_{\perp,0} \rangle$ in various coronal holes, fine scale observations of magnetic fields with high cadence are required; this is one of the suitable targets for Solar-B which is to be launched in 2006.

Acknowledgments. We thank Profs. Kazunari Shibata, Alex Lazarian, and Bruce Tsurutani for many fruitful discussions. This work is in part supported by a Grant-in-Aid for the 21st Century COE “Center for Diversity and Universality in Physics” from the Ministry of Education, Culture, Sports, Science, and Technology (MEXT) of Japan. T.K.S. is supported by the JSPS Research Fellowship for Young Scientists, grant 4607. SI is supported by the Grant-in-Aid (15740118, 16077202) from the MEXT of Japan.

Appendix A: Outgoing Boundary Condition

We introduce our prescription for the outgoing boundary condition of the MHD waves. The method is similar to that in Wu et al. [2001], while ours is implemented for stable treatment of strong MHD shocks.

Basic MHD equations can be expressed in a matrix form as

$$\frac{\partial \mathbf{U}}{\partial t} + A \frac{\partial \mathbf{U}}{\partial r} + \mathbf{C} = 0. \quad (\text{A1})$$

\mathbf{U} and A are explicitly written as

$$\mathbf{U} = \begin{pmatrix} v_r \\ v_{\perp,1} \\ v_{\perp,2} \\ B_{\perp,1} \\ B_{\perp,2} \\ \rho \\ s \end{pmatrix},$$

$$A = \begin{pmatrix} v_r & 0 & 0 & \frac{B_{\perp,1}}{4\pi\rho} & \frac{B_{\perp,2}}{4\pi\rho} & c_s^2/\rho & p/s\rho \\ 0 & v_r & 0 & -\frac{B_r}{4\pi\rho} & 0 & 0 & 0 \\ 0 & 0 & v_r & 0 & -\frac{B_r}{4\pi\rho} & 0 & 0 \\ B_{\perp,1} & -B_r & 0 & v_r & 0 & 0 & 0 \\ B_{\perp,2} & 0 & -B_r & 0 & v_r & 0 & 0 \\ \rho & 0 & 0 & 0 & 0 & v_r & 0 \\ 0 & 0 & 0 & 0 & 0 & 0 & v_r \end{pmatrix},$$

where $s \equiv p/\rho^\gamma$ and $c_s = \sqrt{\gamma p/\rho}$, and subscripts, \perp , 1 and \perp , 2, denote first and second transverse components. \mathbf{C} consists of terms due to external force, additional heating and cooling, and curvature. In our case, we have taken into account gravity, thermal conduction, radiative cooling, and superradial expansion of flux tubes:

$$\mathbf{C} = \begin{pmatrix} F_1 \left(\frac{B_{\perp,1}^2}{4\pi\rho} - v_{\perp,1}^2 \right) + \frac{GM_{\odot}}{r^2} \\ F_1 (v_r v_{\perp,1} - \frac{B_r B_{\perp,1}}{4\pi\rho}) \\ F_1 (v_r v_{\perp,2} - \frac{B_r B_{\perp,2}}{4\pi\rho}) \\ F_1 (B_{\perp,1} v_r - B_r v_{\perp,1}) \\ F_1 (B_{\perp,2} v_r - B_r v_{\perp,2}) \\ F_2 \rho v_r \\ \frac{\rho^{1-\gamma}}{\gamma-1} \left(\frac{1}{\rho r^2 f} \frac{\partial}{\partial r} (r^2 f F_c) + \frac{q_R}{\rho} \right) \end{pmatrix},$$

where $F_1 \equiv \frac{1}{r\sqrt{f}} \frac{\partial}{\partial r} (r\sqrt{f})$ and $F_2 \equiv \frac{1}{r^2 f} \frac{\partial}{\partial r} (r^2 f)$ are arising from the geometrical effect, and $B_{\perp}^2 \equiv B_{\perp,1}^2 + B_{\perp,2}^2$ and $v_{\perp}^2 \equiv v_{\perp,1}^2 + v_{\perp,2}^2$. Please note that \mathbf{C} is negligible except for the thermal conduction term ($\frac{1}{\rho r^2 f} \frac{\partial}{\partial r} (r^2 f F_c)$) in our simulations if r_{out} is set at a sufficiently distant location.

Using eigen values, λ_i ($i = 1, \dots, 7$), and eigen vectors, \mathbf{I}_i , defined as

$$\mathbf{I}_i A = \lambda_i \mathbf{I}_i, \quad (\text{A2})$$

we can derive characteristic equations for the seven MHD waves from eq.(A1) :

$$\mathbf{I}_i \frac{\partial \mathbf{U}}{\partial t} + \lambda_i \mathbf{I}_i \frac{\partial \mathbf{U}}{\partial r} + \mathbf{I}_i \cdot \mathbf{C} = 0 \quad (\text{A3})$$

λ_i corresponds to phase speed of each wave,

$$\lambda_1 = v_r + v_f, \quad \lambda_2 = v_r + v_A, \quad \lambda_3 = v_r + v_s, \quad \lambda_4 = v_r,$$

$$\lambda_5 = v_r - v_s, \quad \lambda_6 = v_r - v_A, \quad \lambda_7 = v_r - v_f, \quad (\text{A4})$$

where $v_f = \sqrt{\frac{1}{2} [c_s^2 + \frac{B^2}{4\pi\rho} + \sqrt{(c_s^2 + \frac{B^2}{4\pi\rho})^2 - 4 \frac{c_s^2 B_{\perp}^2}{4\pi\rho}]}$, $v_A = \frac{B_r}{\sqrt{4\pi\rho}}$, and $v_s = \sqrt{\frac{1}{2} [c_s^2 + \frac{B^2}{4\pi\rho} - \sqrt{(c_s^2 + \frac{B^2}{4\pi\rho})^2 - 4 \frac{c_s^2 B_{\perp}^2}{4\pi\rho}]}$ are phase speeds of fast, Alfvén, and slow modes, respectively. Here we define total magnetic field by $B^2 = B_r^2 + B_{\perp}^2$. The eigen vectors are explicitly written as

$$\mathbf{I}_1 = (\rho v_f (v_f^2 - v_A^2), -\frac{B_r B_{\perp,1}}{4\pi} v_f, -\frac{B_r B_{\perp,2}}{4\pi} v_f,$$

$$\begin{aligned}
 & \frac{B_{\perp,1}^2}{4\pi} v_f^2, \frac{B_{\perp,2}^2}{4\pi} v_f^2, c_s^2(v_f^2 - v_A^2), p/s(v_f^2 - v_A^2)) \\
 \mathbf{I}_2 &= (0, B_{\perp,2}, -B_{\perp,1}, -\frac{B_{\perp,2}}{\sqrt{4\pi\rho}}, \frac{B_{\perp,1}}{\sqrt{4\pi\rho}}, 0, 0) \\
 \mathbf{I}_3 &= (\rho v_s(v_s^2 - v_A^2), -\frac{B_r B_{\perp,1}}{4\pi} v_s, -\frac{B_r B_{\perp,2}}{4\pi} v_s, \\
 & \frac{B_{\perp,1}^2}{4\pi} v_s^2, \frac{B_{\perp,2}^2}{4\pi} v_s^2, c_s^2(v_s^2 - v_A^2), p/s(v_s^2 - v_A^2)) \\
 \mathbf{I}_4 &= (0, 0, 0, 0, 0, 1) \\
 \mathbf{I}_5 &= (\rho v_s(v_s^2 - v_A^2), -\frac{B_r B_{\perp,1}}{4\pi} v_s, -\frac{B_r B_{\perp,2}}{4\pi} v_s, \\
 & -\frac{B_{\perp,1}^2}{4\pi} v_s^2, -\frac{B_{\perp,2}^2}{4\pi} v_s^2, -c_s^2(v_s^2 - v_A^2), -p/s(v_s^2 - v_A^2)) \\
 \mathbf{I}_6 &= (0, B_{\perp,2}, -B_{\perp,1}, \frac{B_{\perp,2}}{\sqrt{4\pi\rho}}, -\frac{B_{\perp,1}}{\sqrt{4\pi\rho}}, 0, 0) \\
 \mathbf{I}_7 &= (\rho v_f(v_f^2 - v_A^2), -\frac{B_r B_{\perp,1}}{4\pi} v_f, -\frac{B_r B_{\perp,2}}{4\pi} v_f, \\
 & -\frac{B_{\perp,1}^2}{4\pi} v_f^2, -\frac{B_{\perp,2}^2}{4\pi} v_f^2, -c_s^2(v_f^2 - v_A^2), -p/s(v_f^2 - v_A^2))
 \end{aligned}$$

The characteristic equations enable us to implement the outgoing boundary condition in a clear and direct manner. All the incoming waves should be removed for the proper outgoing boundary. This is accomplished by setting physical variables, \mathbf{U} , to be constant in space for the incoming characteristics [Thompson, 1987]. Then, we simply impose following condition at $r = r_{\text{out}}$:

$$\left(\mathbf{I}_i \frac{\partial \mathbf{U}}{\partial t} + \mathcal{L}_i + \mathbf{I}_i \cdot \mathbf{C} \right) \Big|_{r_{\text{out}}} = 0, \quad (\text{A5})$$

where

$$\mathcal{L}_i = \begin{cases} \lambda_i \mathbf{I}_i \frac{\partial \mathbf{U}}{\partial r} & : \lambda_i > 0 \text{ (Outgoing)} \\ 0 & : \lambda_i < 0 \text{ (Incoming)} \end{cases} \quad (\text{A6})$$

In our scheme, we firstly perform time evolution to derive \mathbf{U}_j^n ($1 \leq j \leq j_{\text{out}} - 1$) at time n except the outermost grid, j_{out} , from \mathbf{U}_j^{n-1} ($1 \leq j \leq j_{\text{out}}$) at the previous time step, $n - 1$, by the second order MHD Godunov-MOCCT scheme. The physical variables at the outermost grid, $\mathbf{U}_{j_{\text{out}}}^n$ are determined at the end of each time step by using $\mathbf{U}_{j_{\text{out}}}^{n-1}$ and $\mathbf{U}_{j_{\text{out}-1}}^n$. At this time we integrate eq.(A5) implicitly in time for numerical stability:

$$\begin{aligned}
 & (\mathbf{I}_i)_{j_{\text{out}}}^n \frac{\mathbf{U}_{j_{\text{out}}}^n - \mathbf{U}_{j_{\text{out}}}^{n-1}}{\Delta t} \\
 & + (\mathcal{L}_i)_{j_{\text{out}}}^n + (\mathbf{I}_i \cdot \mathbf{C})_{j_{\text{out}}}^n = 0. \quad (\text{A7})
 \end{aligned}$$

We adopt upwind discretization for the spatial derivative appeared in \mathcal{L}_i for the outgoing characteristic, $(\frac{\partial \mathbf{U}}{\partial r})_{j_{\text{out}}}^n = \frac{\mathbf{U}_{j_{\text{out}}}^n - \mathbf{U}_{j_{\text{out}-1}}^n}{\Delta r}$. Note that $(\mathbf{I}_i)_{j_{\text{out}}}^n$, $(\mathcal{L}_i)_{j_{\text{out}}}^n$, and $\mathbf{C}_{j_{\text{out}}}^n$ are functions of $\mathbf{U}_{j_{\text{out}}}^n$, so we need iteration to determine $\mathbf{U}_{j_{\text{out}}}^n$. Equation (A7) determines the physical quantities at the outermost mesh to satisfy the outgoing condition for all the seven MHD characteristics.

We carry out reflection tests for our implementation by using different types of waves with various amplitudes from linear to extremely nonlinear regimes. We here consider two types of waves as typical examples: (i) Alfvén waves, and (ii) oblique fast waves which propagate in 45 degree with respect to the underlying magnetic field. We use Cartesian coordinates with homogeneous background for the tests. Solitary waves which travel in the right direction are initially set, and the outgoing condition is implemented at the right boundary. In order to give the waves which purely propagate in one direction even in the extremely nonlinear regime, we adopt simple wave solutions. Circularly polarized Alfvén waves

traveling in one direction are the exact solutions of the basic MHD equations. For the oblique fast waves, ρ , p , v_x , and v_y can be expressed by B_y [Wu, 1987]:

$$\frac{d\rho}{dB_y} = \frac{B_y}{4\pi} \frac{1}{v_f^2 - c_s^2}, \quad (\text{A8})$$

$$\frac{dv_x}{dr} = \frac{B_y}{4\pi\rho} \frac{v_f}{v_f^2 - c_s^2}, \quad (\text{A9})$$

$$\frac{dv_y}{dB_y} = -\frac{B_x}{4\pi\rho v_f}, \quad (\text{A10})$$

$$\frac{dp}{dB_y} = \frac{B_y}{4\pi} \frac{c_s^2}{v_f^2 - c_s^2}. \quad (\text{A11})$$

Note that we can treat fast (and slow) waves in two dimensional (x & y) space without loss of generality because they are coplanar, while the three dimensional space is required for circularly polarized Alfvén waves. We initially give sinusoidal variations of B_y for the fast waves and the other quantities are determined by Equations (A8) - (A11). If the wave amplitude, δv , is sufficiently smaller than v_f , all the quantities can be approximated by sinusoidal variations.

Figure 15 shows an example of the reflection tests for the oblique fast waves. We non-dimensionalize the B values by $1/4\pi \rightarrow 1$. The initial background conditions are, $\rho = 1$, $p = 1$, $B_x = 1.5$, $B_y = 1.5$, $v_x = 0$, and $v_y = 0$, which give plasma β value, $\beta = 2p/B^2 (= 8\pi p/B^2 \text{ in cgs-Gauss unit}) = 0.44$. We give magnetic field amplitude, $\delta B_y = 6.5$, which corresponds to relatively strong non-linearity, $\delta v/v_f = 3.1$. The simulation box is from $x = 0$ to $x = 4$ and the number of grid points is 512. The initial solitary wave is put between $x = 2$ and 3. The initial condition ($t = 0$) and results at $t = 0.6$ are plotted in dashed and solid lines. To estimate errors at the right boundary, we also carry out simulation in larger box between $x = 0$ and 8 (dotted lines), which is free from the boundary errors at $x = 4$.

Because of the strong nonlinearity, the wave rapidly steepens to form shocks before reaching $x = 4$. These shocks travel to the right direction, which are seen in the simulation with the larger box size (dotted lines). At $t = 0.6$, the main part of the wave goes out of the simulation box ($x = 4$) except the trailing edge. The differences between solid and dotted lines indicate errors due to our implementation of the outflow boundary condition. Figure 15 shows the errors are quite small; relative errors to the initial amplitude are at most 1% for each variable. Our implementation is good enough for the passage of the moderately strong shocks.

Figure 16 shows the relative errors to the initial amplitude, $\delta v_{\text{error}}/\delta v$ on the normalized wave amplitude, $\delta v/v_f$ and $\delta v/v_A$, for the oblique fast waves and circularly polarized Alfvén waves. As for the relative errors, we plot the errors of v_y , whereas the other quantities (ρ, p, B_y, v_x) give similar results. If $\delta v/v_{\text{ph}} \lesssim 3$ ($v_{\text{ph}} = v_f$ or v_A is phase speed), the relative errors are smaller than 0.01 and our implementation is sufficiently acceptable. The Alfvén wave with $\delta v/v_A = 10$ gives larger $\delta v_{\text{error}}/\delta v \simeq 0.05$. This is because as the wave travels it does not only consist of Alfvén modes but contains non-linear fast and slow wave components. However, this value ($\delta v_{\text{error}}/\delta v \simeq 0.05$) is still acceptable since an error in energy ($\propto \delta v^2$) is only 0.3%.

Notes

1. It is instructive to note that the incoming Alfvén waves have the positive correlation between v_{\perp} and B_{\perp} (dark-dark or light-light in the figures), while the outgoing modes have the negative correlation (dark-light or light-dark).
2. The phase correlation of the longitudinal slow waves is opposite to that of the transverse Alfvén waves. The outgoing slow modes have the positive correlation between amplitudes of v_r and ρ , ($\delta v_r \delta \rho > 0$), while the incoming modes have the negative correlation ($\delta v_r \delta \rho < 0$).

References

- Anderson, C. S. & Athay, R. G. (1989), Chromospheric and coronal heating, *Astrophys. J.*, , 336, 1089 - 1091

- Axford, W. I. & McKenzie, J. F. (1997), The Solar Wind in "Cosmic Winds and the Heliosphere", Eds. Jokipii, J. R., Sonnet, C. P., and Giampapa, M. S., University of Arizona Press, 31 - 66
- Banerjee, D., Teriaca, L., Doyle, J. G., & Wilhelm, K. (1998), Broadening of SI VIII lines observed in the solar polar coronal holes, *Astron. Astrophys.*, , 339, 208 - 214
- Barnes, A. (1966), Collisionless damping of hydromagnetic waves, *Phys. Fluid*, 9, 1483
- Bogdan, T. J. et al. (2003), Waves in the magnetized solar atmosphere. II. waves from localized sources in magnetic flux concentrations, *Astrophys. J.*, , 500, 626 - 660
- Boynton, G. C. & Torkelsson, U. (1996), Dissipation of non-linear Alfvén waves, *Astron. Astrophys.*, , 308, 299 - 308
- Braginskii, S. I. (1965), Transport Processes in a Plasma, *Rev. Plasma Phys.*, 1., 205 - 311
- Canals, A., Breen, A. R., Ofman, L., Moran, P. J., & Fallows, R. A. (2002), Estimating random transverse velocities in the fast solar wind from EISCAT interplanetary scintillation measurements, *Ann. Geophys.*, 20, 1265 - 1277
- Carlsson, M. & Stein, R. F. (1992), Non-LTE radiating acoustic shocks and CA II K2V bright points, *Astrophys. J.*, , 397, L59 - L62
- Cho, J. & Lazarian, A. (2002), Compressible Sub-Alfvénic MHD Turbulence in Low- β Plasmas, *Phys. Rev. Lett.*, , 88, 245001
- Cho, J. & Lazarian, A. (2003), Compressible magnetohydrodynamic turbulence: mode coupling, scaling relations, anisotropy, viscosity-damped regime and astrophysical implications, *Mon. Not. R. Astron. Soc.*, , 345, 325 - 339
- Cranmer, S. R. (2000), Ion cyclotron wave dissipation in the solar corona: *Astrophys. J.*, , 532, 1197 - 1208
- Cranmer, S. R. & van Ballegoijen, A. A. (2005), On the Generation, Propagation, and Reflection of Alfvén Waves from the Solar Photosphere to the Distant Heliosphere, *Astrophys. J. (Supp.)*, , 156, 265 - 293
- Crooker, N. U., Shodhan, S., Cosling, J. T., Simmerer, J., Lepping, R. P., Steinberg, J. T., & Kahler, S. W. (2000), Density extremes in the solar wind, *Geophys. Res. Lett.*, , 27, 3769 - 3772
- De Moortel, I., Hood, A. W., & Arber, T. D. (2000), Phase mixing of Alfvén waves in a stratified and radially diverging, open atmosphere, *Astron. Astrophys.*, , 354, 334 - 348
- Dusenbery, P. B. & Hollweg J. V. (1981), Ion-cyclotron heating and acceleration of solar wind minor ions, *J. Geophys. Res.*, , 86, 153 - 164
- Endeve, E., Leer, E., & Holtzer, T. E. (2003), Two-dimensional Magnetohydrodynamic Models of the Solar Corona: Mass Loss from the Streamer Belt, *Astrophys. J.*, , 589, 1040 - 1053
- Esser, R., Habbal, S. R., Colse, W. A., & Hollweg, J. (1997), Hot protons in the inner corona and their effect on the flow properties of the solar wind, *J. Geophys. Res.*, , 102, 7063 - 7074
- Esser, R., Fineschi, S., Dobrzycka, D., Habbal, S. R., Edgar, R. J., Raymond, J. C., & Kohl, J. L. (1999), Plasma properties in coronal holes derived from measurements of minor ion spectral lines and polarized white light intensity, *Astrophys. J.*, , 510, L63 - L67
- Fisk, L. A., Schwadron, N. A., & Zurbuchen, T. H. (1999), Acceleration of the fast solar wind by the emergence of new magnetic flux, *J. Geophys. Res.*, , 104, A4, 19765 - 19772
- Fludra, A., Del Zanna, G., & Bromage, B. J. I. (1999), EUV observations above polar coronal holes, *Spa. Sci. Rev.*, 87, 185 - 188
- Goldreich, P. & Sridhar, S. (1995), Toward a theory of interstellar turbulence. 2: Strong Alfvénic turbulence, *Astrophys. J.*, , 438, 763 - 775
- Goldstein, M. L. (1978), An instability of finite amplitude circularly polarized Alfvén waves, *Astrophys. J.*, , 219, 700 - 704
- Grall, R. R., Coles, W. A., Klinglesmith, M. T., Breen, A. R., Williams, P. J. S., Markkanen, J., & Esser, R. (1996), Rapid acceleration of the polar solar wind, *Nature*, 379, 429 - 432
- Grappin, R., Léorat, J., & Habbal, S. R. (2002), Large-amplitude Alfvén waves in open and closed coronal structures: A numerical study, *J. Geophys. Res.*, , 107, A11, SSH 16-1
- Geiss, J. et al. (1995), The southern high-speed stream : results from the SWICS instrument on Ulysses, *science*, 268, 1033 - 1036
- Habbal, S. R., Esser, R., Guhathakura, M., & Fisher, R. R. (1994), Flow properties of the solar wind derived from a two-fluid model with constraints from white light and in situ interplanetary observations, *Geophys. Res. Lett.*, , 22, 1465 - 1468
- Hasegawa, A. & Lui, C. (1975), Kinetic process of plasma heating due to Alfvén wave excitation, *Phys. Rev. Lett.*, , 35, 370 - 373
- Hayes, A. P., Vourlidas, A., & Howard, R. A. (2001), Deriving the Electron Density of the Solar Corona from the Inversion of Total Brightness Measurements, *Astrophys. J.*, , 548, 1081
- Heyvaerts, J. & Priest, E. R. (1983), Coronal heating by phase-mixed shear Alfvén waves, *Astron. Astrophys.*, , 117, 220 - 234
- Hollweg, J. V. (1982), Heating of the corona and solar wind by switch-on shocks, *Astrophys. J.*, , 254, 806 - 813
- Holweger, H., Gehlsen, M., & Ruland, F. (1978), Spatially-averaged properties of the photospheric velocity field, *Astron. Astrophys.*, , 70, 537 - 542
- Jacques, S. A. (1977), Momentum and energy transport by waves in the solar atmosphere and solar wind, *Astrophys. J.*, , 215, 942 - 951
- Katsukawa, Y. & Tsuneta, S. (2001), Small Fluctuation of Coronal X-Ray Intensity and a Signature of Nanoflares, *Astrophys. J.*, , 557, 343 - 350
- Kohl, J. L. et al. (1998), UVCS/SOHO empirical determinations of anisotropic velocity distributions in the solar corona, *Astrophys. J.*, , 501, L127 - L 131
- Kojima, M., Fujiki, K., Ohmi, T., Tokumaru, M., Yokobe, A., & Hakamada, K. (1999), Low-speed solar wind from the vicinity of solar active regions, *J. Geophys. Res.*, , 104, 16993 - 17004
- Kojima, M., Breen, A. R., Fujiki, K., Hayashi, K., Ohmi, T., & Tokumaru, M. (2004), Fast solar wind after the rapid acceleration, *JGRA*, 109, A04103, 2004
- Kojima, M., K. Fujiki, M. Hirano, M. Tokumaru, T. Ohmi, and K. Hakamada, (2005), Solar Wind properties from IPS observations, "The Sun and the heliosphere as an Integrated System", Giannina Poletto and Steven T. Suess, Eds. Kluwer Academic Publishers, 147 - 181
- Kopp, R. A. & Holzer, T. E. (1976), Dynamics of coronal hole regions. I - Steady polytropic flows with multiple critical points, *Sol. Phys.*, 49, 43 - 56
- Kudoh, T. & Shibata, K. (1999), Alfvén wave model of spicules and coronal heating, *Astrophys. J.*, , 514, 493 - 505
- Lamers, H. J. G. L. M. & Cassinelli, J. P. (1999), 'Introduction to Stellar Wind', Cambridge
- Lamy, P., Quemerais, E., Liebaria, A., Bout, M., Howard, R., Schwenn, R., & Simnett, G. (1997), Characterization of Polar Plumes from LASCO-C2 Images in Early 1996, in Fifth SOHO Workshop, The Corona and Solar Wind near Minimum Activity, ed A. Wilson (ESA-SP 404; Noordwijk:ESA), 491
- Landini, M. & Monsignori-Fossi, B. C. (1990), The X-UV spectrum of thin plasmas, *A&A Supp.*, 82, 229 - 260
- Lau, Y.-T. & Sireger, E. (1996), Nonlinear Alfvén Wave Propagation in the Solar Wind, *Astrophys. J.*, , 465, 451 - 461
- Lazarian, A., Vishniac, E. T., & Cho, J. (2004), Magnetic field structure and stochastic reconnection in a partially ionized plasma, *Astrophys. J.*, , 603, 180
- Le, G., Russell, C. T., & Petrinc, S. M. (2000), The magnetosphere on May 11, 1999, the day the solar wind almost disappeared: I. Current systems, *Geophys. Res. Lett.*, , 27, 1827 - 1830
- Lie-Svendensen, Ø, Leer, E., & Hansteen, V. H. (2001), A 16-moment solar wind model: From the chromosphere to 1 AU *J. Geophys. Res.*, , 106, 8217 - 8232
- Lithwick, Y. & Goldreich, P. (2003), Imbalanced weak magnetohydrodynamic turbulence, *Astrophys. J.*, , 582, 1220 - 1240
- Marsch, E., Schwenn, R., Rosenbauer, H., Muehlhaeuser, K.-H., Pilipp, W., & Neubauer, F. M. (1982), Solar wind protons - Three-dimensional velocity distributions and derived plasma parameters measured between 0.3 and 1 AU, *J. Geophys. Res.*, , 87, 52-72
- Marsch, E., Goertz, C. K., & Richter, K. (1982), Wave heating and acceleration of solar wind ions by cyclotron resonance, *J. Geophys. Res.*, , 87, 5030 - 5044
- Matthaeus, W. H., Zank, G. P., Oughton, S., Mullan, D. J., & Dmitruk, P. (1999), Coronal heating by magnetohydrodynamic turbulence driven by reflected low-frequency waves, *Astrophys. J.*, , 523, L93 - L96
- Miyagoshi, T., Isobe, T., Yokoyama, T., & Shibata, K. (2005), in preparation
- Moore, R. L., Suess, S. T., Musielak, Z. E., & An, A.-H. (1991), Alfvén wave trapping, network microflaring, and heating in solar coronal holes, *Astrophys. J.*, , 378, 347 - 359
- Moriyasu, S., Kudoh, T., Yokoyama, T., & Shibata, K. (2004), The nonlinear Alfvén wave model for solar coronal heating and nanoflares, *Astrophys. J.*, , 601, L107 - L110
- Nakagawa, T., Gopalswamy, N., & Yashiro, S. (2005), Solar wind speed within $20R_{\odot}$ of the sun estimated from limb CMEs, submitted to *J. Geophys. Res.*,
- Nakariakov, V. M., Roberts, B., & Murawski, K. (1998), Nonlinear coupling of MHD waves in inhomogeneous steady flows, *Astron. Astrophys.*, , 332, 795 - 804, 1998
- Ofman, L. & Davila, J. M. (1997), Solar Wind Acceleration by Solitary Waves in Coronal Holes, *Astrophys. J.*, , 476, 357 - 365
- Ofman, L. & Davila, J. M. (1998), Solar wind acceleration by large-amplitude nonlinear waves: Parametric study, *J. Geophys. Res.*, , 103, 23677 - 23690

- Ofman, L., Nakariakov, V. M., & Deforest, C. E. (1999), Slow magnetosonic waves in coronal plumes, *Astrophys. J.*, , 514, 441 - 447
- Ofman, L. (2004), Three-fluid model of the heating and acceleration of the fast solar wind, *J. Geophys. Res.*, , 109, A07102
- Orta, J. A., Huerta, M. A., & Boynton, G. C. (2003), Magnetohydrodynamic Shock Heating of the Solar Corona, *Astrophys. J.*, , 596, 646 - 655
- Oughton, S., Matthaeus, W. H., Dmitruk, P., Milano, L. J., Zank, G. P., & Mullan, D. J. (2001), A reduced magnetohydrodynamic model of coronal heating in open magnetic regions driven by reflected low-frequency Alfvén waves, *Astrophys. J.*, , 551, 565 - 575
- Parenti, S., Bromage, B. J. I., Poletto, G., Noci, G., Raymond, J. C., & Bromage, G. E. (2000), Characteristics of solar coronal streamers. Element abundance, temperature and density from coordinated CDS and UVCS SOHO observations, *Astron. Astrophys.*, , 363, 800
- Parnell, C. E. & Jupp, P. E. (2000), Statistical Analysis of the Energy Distribution of Nanoflares in the Quiet Sun, *Astrophys. J.*, , 529, 554 - 569
- Phillips, J. L. et al. (1995), Ulysses solar wind plasma observations from pole to pole. *Geophys. Res. Lett.*, , 22, 3301 - 3304
- Raouafi, N.-E. & Solanki, S. K. (2004), Effect of the Electron Density Stratification on Off-Limb O IV Line Profiles : How Large Is the Velocity Distribution Anisotropy in the Solar Corona ?, *Astron. Astrophys.*, , 427, 725 - 733
- Richardson, I. G., Berdichevsky, D., Desch, M. D., & Farrugia, C. J. (2000), Solar-cycle variation of low density solar wind during more than three solar cycles, *Geophys. Res. Lett.*, , 27, 3761 - 3764
- Sakurai, T., Ichimoto, K., Raju, K. P., & Singh, J. (2002), Spectroscopic Observation of Coronal Waves, *Sol. Phys.*, , 209, 265 - 286
- Sandbæk, Ø. & Leer, E. (1995), Coronal Heating and Solar Wind Energy Balance, *Astrophys. J.*, , 454, 486 - 498
- Sano, T. & Inutsuka, S. (2006), in preparation
- Schwadron, N. A. & McComas, D. J. (2003), Solar Wind Scaling Law, *Astrophys. J.*, , 599, 1395 - 1403
- Sheeley, N. R. Jr. et al. (1997), Measurements of Flow Speeds in the Corona between 2 and 30 R_{\odot} , *Astrophys. J.*, , 484, 472
- Smith, C. W., Mullan, D. J., Ness, N. F., Skoug, R. M., & Steinberg, J. (2001), Day the solar wind almost disappeared: Magnetic field fluctuations, wave refraction and dissipation, *J. Geophys. Res.*, , 106, 18625 - 18634
- Sturrock, P. A. (1999), Chromospheric Magnetic Reconnection and Its Possible Relationship to Coronal Heating, *Astrophys. J.*, , 521, 451 - 459
- Suzuki, T. K. (2004), Coronal heating and acceleration of the high/low-speed solar wind by fast/slow MHD shock trains, *Mon. Not. R. Astron. Soc.*, , 349, 1227 - 1239
- Suzuki, T. K. & Inutsuka, S. (2005), Making the corona and the fast solar wind: a self-consistent simulation for the low-frequency Alfvén waves from photosphere to 0.3AU, *Astrophys. J.*, , 632, L49 - L52
- Suzuki, T. K., Yan, H., Lazarian, A., Cassinelli, J. P. (2006), Collisionless Damping of Fast MHD Waves in Magneto-rotational Winds, *Astrophys. J.*, , in press
- Suzuki, T. K. (2006), Forecasting Solar Wind Speeds, *Astrophys. J.*, , 640, L75 - L78
- Terasawa, T., Hoshino, M., Sakai, J. I., & Hada, T. (1986), Decay instability of finite-amplitude circularly polarized Alfvén waves: A numerical simulation of stimulated Brillouin scattering, *J. Geophys. Res.*, , 91, 4171
- Teriaca, L., Poletto, G., Romoli, M., & Biasecker, D. A. (2003), The nascent solar wind: origin and acceleration, *Astrophys. J.*, , 588, 566 - 577
- Thompson, K. W. (1987), Time dependent boundary conditions for hyperbolic systems, *J. Computational. Phys.*, , 68, 1
- Tsiklauri, D., Sakai, J.-T., & Saito, S. (2005), Particle-In-Cell simulations of circularly polarised Alfvén wave phase mixing: A new mechanism for electron acceleration in collisionless plasmas, *Astron. Astrophys.*, , 435, 1105 - 1113
- Tsuneta, S., Hara, H., Shimizu, T., Acton, L. W., Strong, K. T., Hudson, H. S., & Ogawara, Y. (1992), Observation of a solar flare at the limb with the YOHKOH Soft X-ray Telescope, *PASJ*, 44, L63 - L69
- Tsurutani, B. T. & Ho, C. M. (1999), A review of discontinuities and Alfvén waves in interplanetary space: Ulysses results, *Rev. Geophys.*, , 37, 517 - 524
- Tsurutani, B. T. et al. (2002), Relationship between discontinuities, magnetic holes, magnetic decreases and nonlinear Alfvén waves: Ulysses observations over the solar poles, *Geophys. Res. Lett.*, , 29, 23-1
- Tsurutani, B. T., Lakhina, G. S., Pickett, J. S., Guarnieri, F. L., Lin, N., & Goldstein, B. E. (2005), Nonlinear Alfvén waves, discontinuities, proton perpendicular acceleration, and magnetic holes/decreases in interplanetary space and the magnetosphere: intermediate shocks?, *Nonlinear Processes in Geophysics*, 21, 321 - 336
- Tu, C.-Y., Zhou, C., Marsch, E., Xia, L.-D., Zhao, L., Wang, J.-X., & Wilhelm, K. (2005), Solar Wind Origin in Coronal Funnels, *Science*, 308, 519 - 523
- Ulrich, R. K. (1996), Observations of Magnetohydrodynamic Oscillations in the Solar Atmosphere with Properties of Alfvén Waves, *Astrophys. J.*, , 465, 436 - 450
- Usmanov, A. V., Goldstein, M. L., & Farrell, W. M. (2000), A view of the inner heliosphere during the May 10-11, 1999 low density anomaly *Geophys. Res. Lett.*, , 27, 3765
- Wang, Y.-M. & Sheeley, Jr, N. R. (1990), Solar wind speed and coronal flux-tube expansion, *Astrophys. J.*, , 355, 726 - 732
- Wang, Y.-M. & Sheeley, Jr, N. R. (1991), Why fast solar wind originates from slowly expanding coronal flux tubes, *Astrophys. J.*, , 372, L45 - L48
- Wang, Y.-M., Sheeley, N. R., Socker, D. G., Howard, R. A., Rich, N. B. (2000), *J. Geophys. Res.*, , 105, 25133
- Wilhelm, K., Marsch, E., Dwivedi, B. N., Hassler, D. M., Lemaire, P., Gabriel, A. H., & Huber, M. C. E. (1998), The solar corona above polar coronal holes as seen by SUMER on SOHO, *Astrophys. J.*, , 500, 1023 - 1038
- Wu, C. C. (1987), On MHD intermediate shocks, *Geophys. Res. Lett.*, , 14, 668 - 671
- Wu, S. T., Zheng, H., Wang, S., Thompson, B. J., Plunkett, S. P., Zhao, X. P., Dryer, M. (2001), Three-dimensional numerical simulation of MHD waves observed by the Extreme Ultraviolet Imaging Telescope, *J. Geophys. Res.*, , A11, 25089 - 25102
- Yan, H. & Lazarian, A. (2004), Cosmic-Ray Scattering and Streaming in Compressible Magnetohydrodynamic Turbulence, *Astrophys. J.*, , 614, 757-769
- Zangrilli, L., Poletto, G., Nicolosi, P., Noci, G., & Romoli, M. (2002), Two-dimensional structure of a polar coronal hole at solar minimum: new semiempirical methodology for deriving plasma parameters. *Astrophys. J.*, , 574, 477 - 494

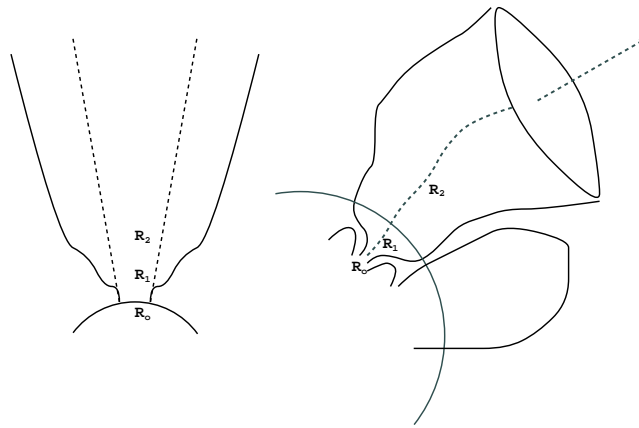


Figure 1. The left figure shows the geometry of the open flux tube in our simulations. Arch represents the solar surface and solid lines indicates magnetic field lines. Dashed lines correspond to radial expansion. The flux tube expands super-radially around R_1 and R_2 . This geometry mimics realistic open flux tubes on the sun. An example is shown on the right. A sizable fraction of the surface is occupied by closed loops with a typical length $\sim 10^4$ km ($=0.014R_\odot$). Above that height open structures become more dominant. Then, the open flux tube expands super-radially at $\sim R_1 (= 1.01R_\odot$ in our simulations). The tube further expands at $\sim R_2 (= 1.2R_\odot$ in our simulations) due to the large-scale dipole structure.

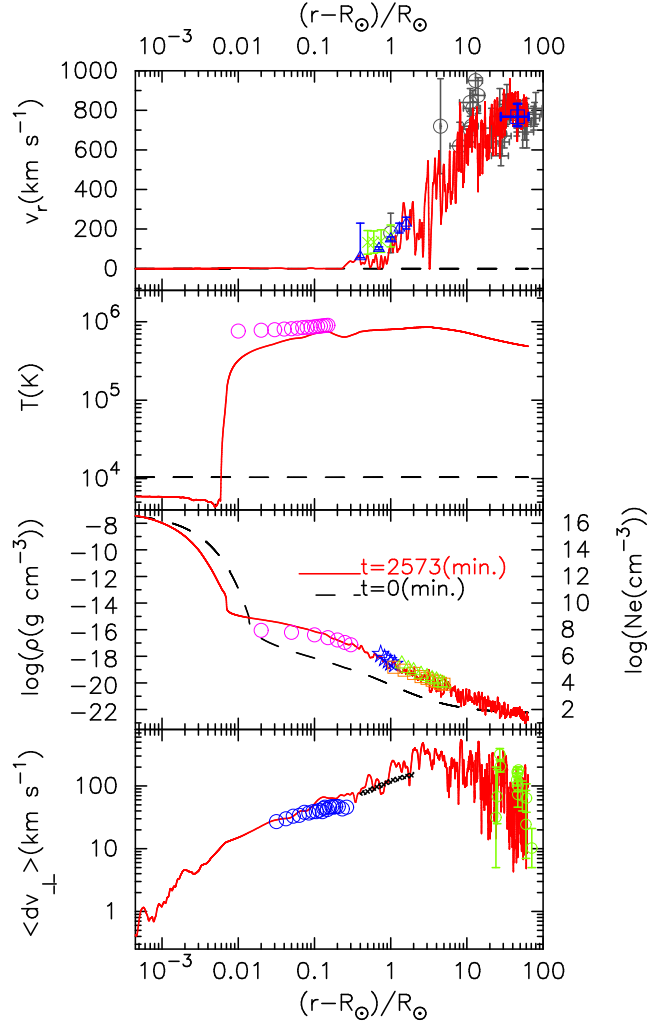


Figure 2. Results of Run I with observations of fast solar wind. From top to bottom, outflow speed, v_r (km s^{-1}), temperature, T (K), density in logarithmic scale, $\log(\rho)$ (g cm^{-3}), and rms transverse amplitude, $\langle dv_{\perp} \rangle$ (km s^{-1}) are plotted. Observational data in the third panel are electron density, $\log(N_e)$ (cm^{-3}) which is to be referred to the right axis. Dashed lines indicate the initial conditions and solid lines are the results at $t = 2573$ minutes. In the bottom panel, the initial value ($\langle dv_{\perp} \rangle = 0$) does not appear. *first:* Green vertical error bars are proton outflow speeds in an interplume region by UVCS/SoHO [Teriaca et al., 2003]. Dark blue vertical error bars are proton outflow speeds by the Doppler dimming technique using UVCS/SoHO data [Zangrilli et al., 2002]. A dark blue open square with errors is velocity by IPS measurements averaged in 0.13 - 0.3AU of high-latitude regions [Kojima et al., 2004]. Light blue data are taken from Grall et al. [1996]; crossed bars are IPS measurements by EISCAT, crossed bars with open circles are by VLBA measurements, and vertical error bars with open circles are data based on observation by SPARTAN 201-01 [Habbal et al., 1994]. *second:* Pink circles are electron temperatures by CDS/SoHO [Fludra et al., 1999]. *third:* Circles and stars are observations by SUMER/SoHO [Wilhelm et al., 1998] and by CDS/SoHO [Teriaca et al., 2003], respectively. Triangles [Teriaca et al., 2003] and squares [Lamy et al., 1997] are observations by LASCO/SoHO. *fourth:* Blue circles are non-thermal broadening inferred from SUMER/SoHO measurements [Banerjee et al., 1998]. Cross hatched region is an empirical constraint of non-thermal broadening based on UVCS/SoHO observation [Esser et al., 1999]. Green error bars are transverse velocity fluctuations derived from IPS measurements by EISCAT [Canals et al., 2002].

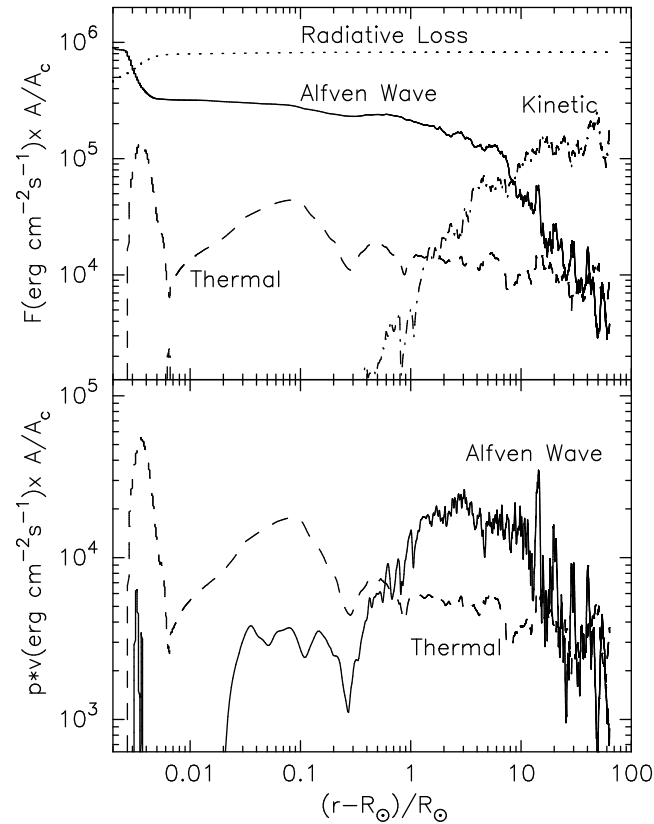


Figure 3. Energy flux (top) and momentum flux (bottom) as a function of distance from the photosphere. Each component is averaged with respect to time during 28min (the longest wave period considered). Each value is normalized by cross section, A_c , of the flow tube at $r = r_c (= 1.02R_\odot)$; note that the real flux is larger (smaller) in $r < r_c$ ($r > r_c$). *top:* Solid, dashed, dot-dashed, and dotted lines denote the energy flux of the Alfvén wave, the enthalpy flux, the kinetic energy flux, and the integrated radiative loss. *bottom* Solid and dashed lines indicate the advected pressure terms of the Alfvén waves, $\langle p_A v_r \rangle$ and the thermal pressure, $\langle p v_r \rangle$.

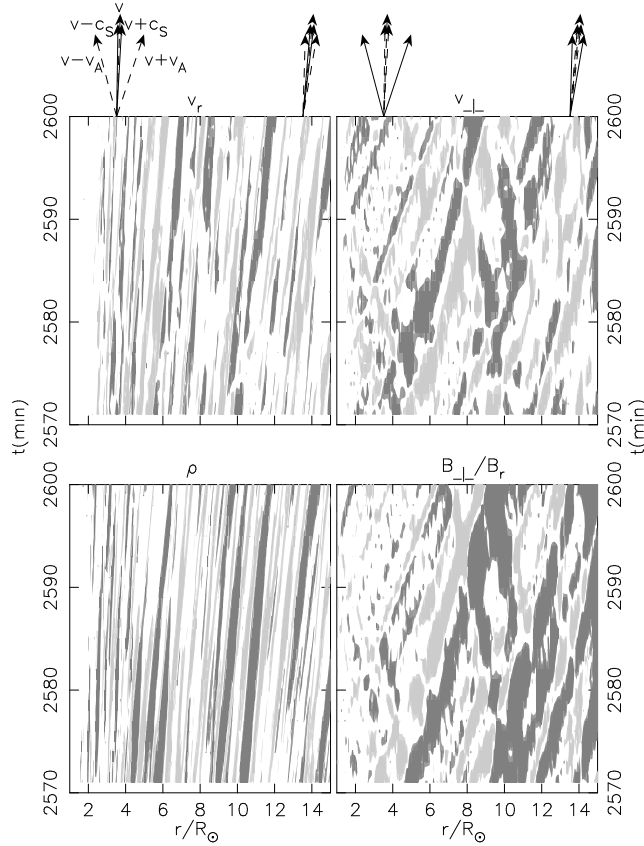


Figure 4. $r - t$ diagrams for v_r (upper-left), ρ (lower-left), v_{\perp} (upper-right), and B_{\perp}/B_r (lower-right.) The horizontal axes cover from R_{\odot} to $15R_{\odot}$, and the vertical axes cover from $t = 2570$ minutes to 2600 minutes. Dark and light shaded regions indicate positive and negative amplitudes which exceed certain thresholds. The thresholds are $dv_r = \pm 96 \text{ km/s}$ for v_r , $d\rho/\rho = \pm 0.25$ for ρ , $v_{\perp} = \pm 180 \text{ km/s}$ for v_{\perp} , and $B_{\perp}/B_r = \pm 0.16$ for B_{\perp}/B_r , where $d\rho$ and dv_r are differences from the averaged ρ and v_r . Arrows on the top panels indicate characteristics of Alfvén, slow MHD and entropy waves at the respective locations (see text).

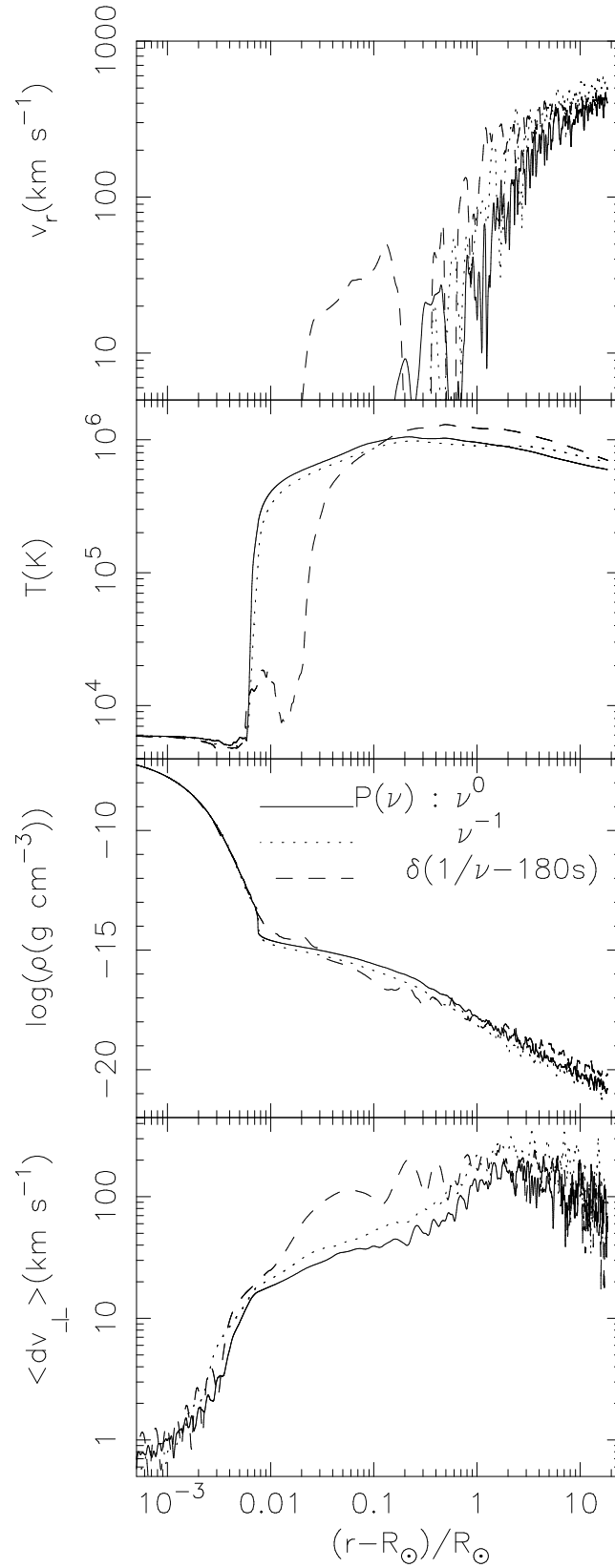


Figure 5. Structures of corona and solar wind for various fluctuation spectrums at the photosphere. From top to bottom, we plot solar wind speed, v_r (km s^{-1}), temperature, T (K), density in logarithmic scale, $\log(\rho(\text{g cm}^{-3}))$, and rms transverse velocity, $\langle dv_{\perp} \rangle$ (km s^{-1}). Dotted, solid, and dashed lines are results of $P(\nu) \propto \nu^{-1}$ (Run II), ν^0 (Run III), and $\delta(1/\nu - 180\text{s})$ (Run IV), respectively. Each variable is averaged with respect to time during 28min (the longest wave period considered).

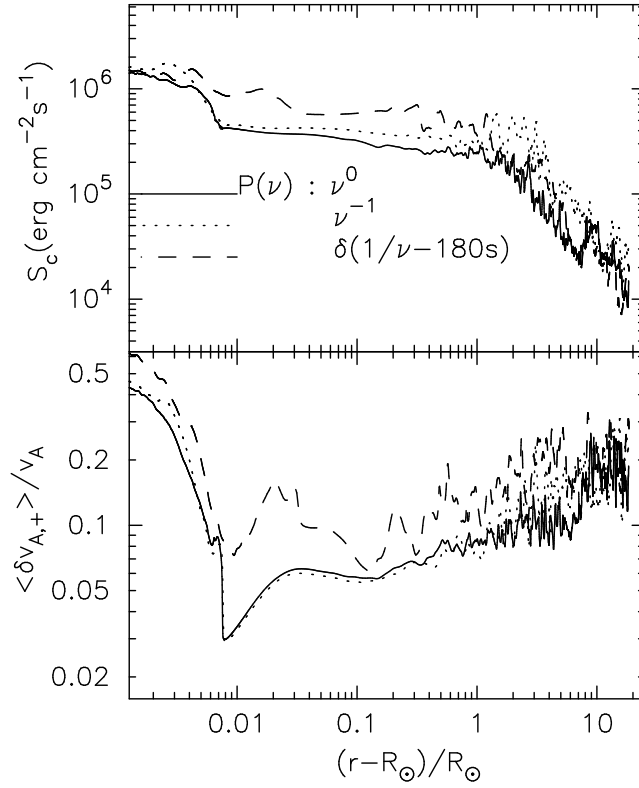


Figure 6. Adiabatic constant, $S_c(\text{erg cm}^{-2}\text{s}^{-1})$, (top) and normalized amplitude, $\langle \delta v_{A,+} \rangle / v_A$, (bottom) of outgoing Alfvén waves for various spectrums. Dotted, solid, and dashed lines are results of $P(\nu) \propto \nu^{-1}$ (Run II), ν^0 (Run III), and $\delta(1/\nu - 180\text{s})$ (Run IV), respectively. Each variable is averaged with respect to time during 28min (the longest wave period considered).

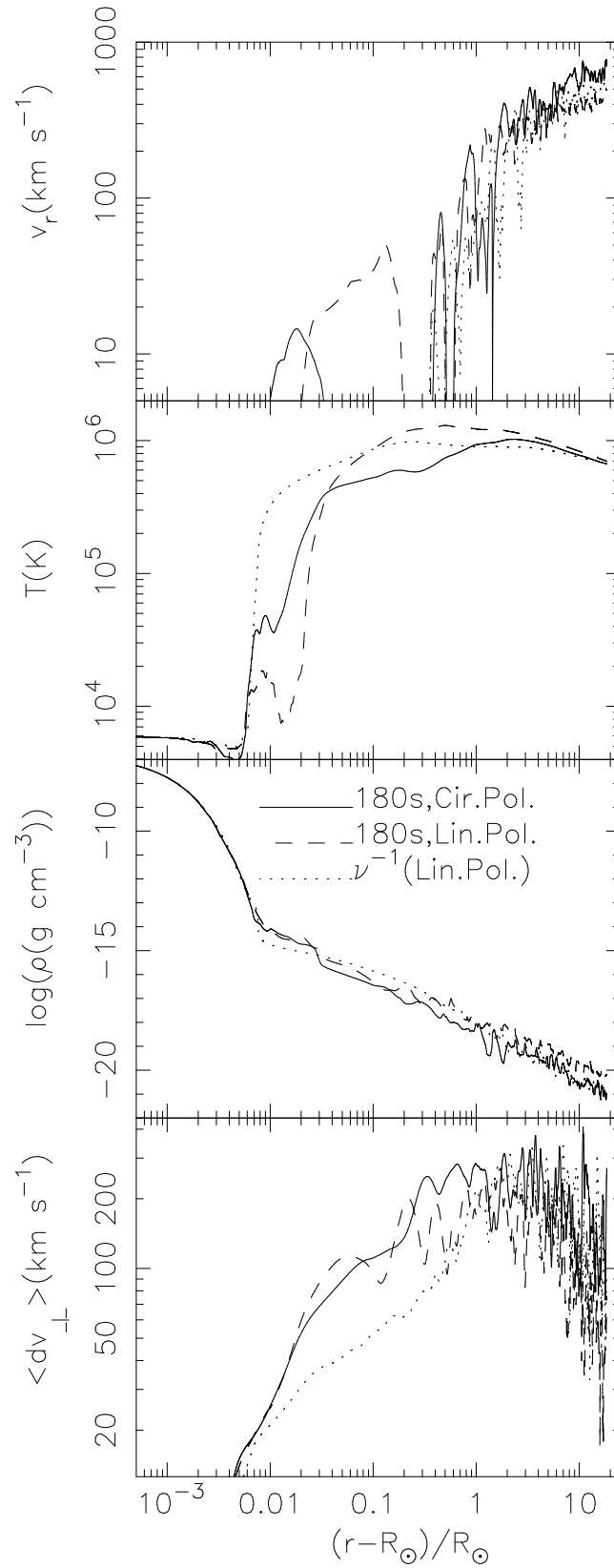


Figure 7. Same as Figure 5 but for different polarizations of the perturbations. Solid, dashed, and dotted lines are results of circularly polarized sinusoidal waves (Run V), linearly polarized sinusoidal waves (Run IV), and linearly polarized waves with power spectrum, $P(\nu) \propto \nu^{-1}$ (Run II), respectively.

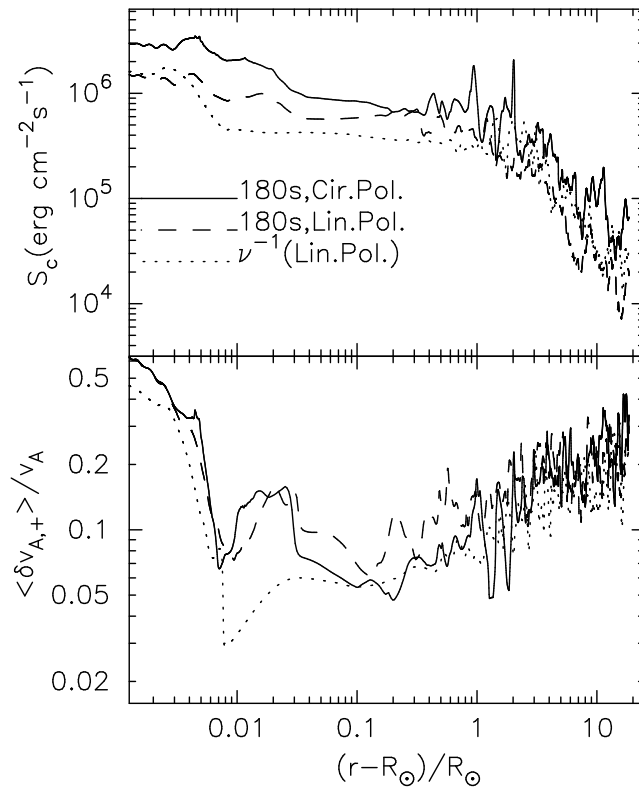


Figure 8. Same as Figure 6 but for different polarizations of the perturbations. Solid, dashed, and dotted lines are results of circular polarized sinusoidal waves (Run V), linearly polarized sinusoidal waves (Run IV), and linearly polarized waves with power spectrum, $P(\nu) \propto \nu^{-1}$ (Run II), respectively.

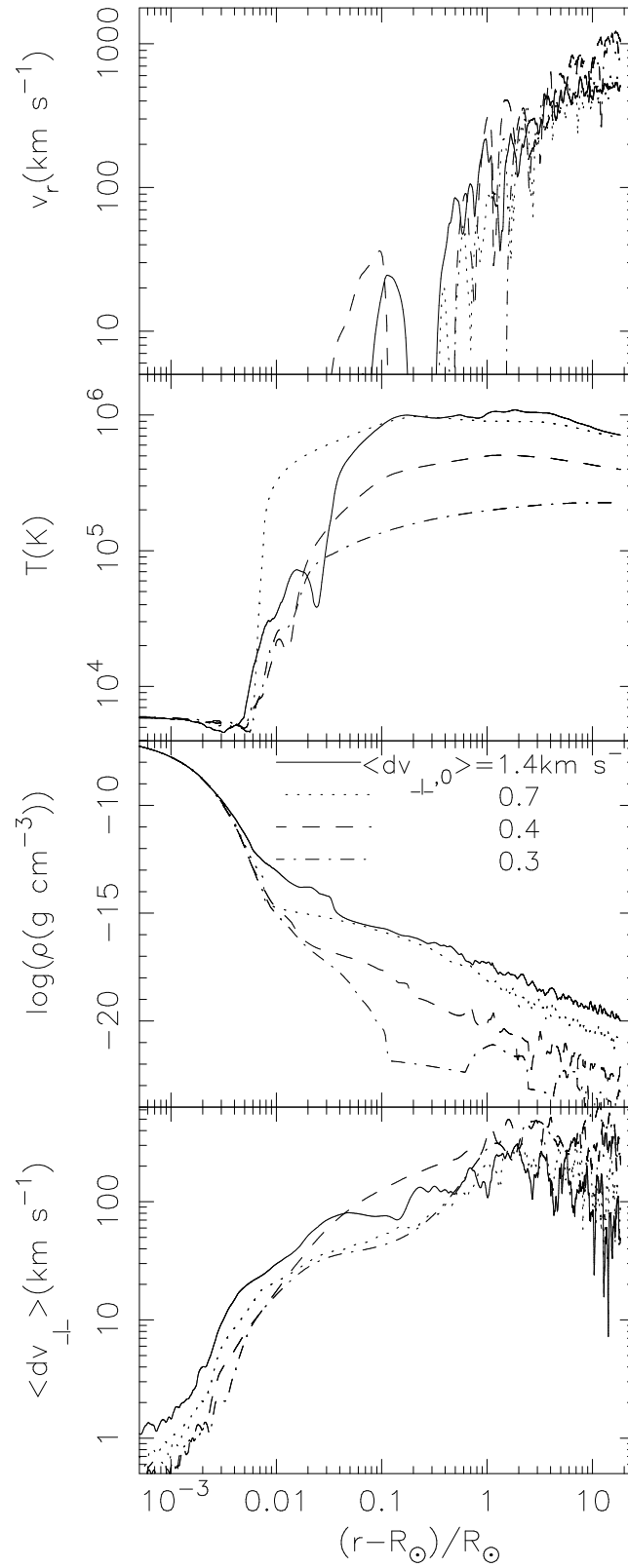


Figure 9. Same as Figure 5 but for different $\langle dv_{\perp,0} \rangle$. Solid, dotted, dashed, and dot-dashed lines are results of $\langle dv_{\perp,0} \rangle = 1.4$ (Run VI), 0.7 (Run II), 0.4 (Run VII), and $0.3(\text{km s}^{-1})$ (Run IX), respectively.

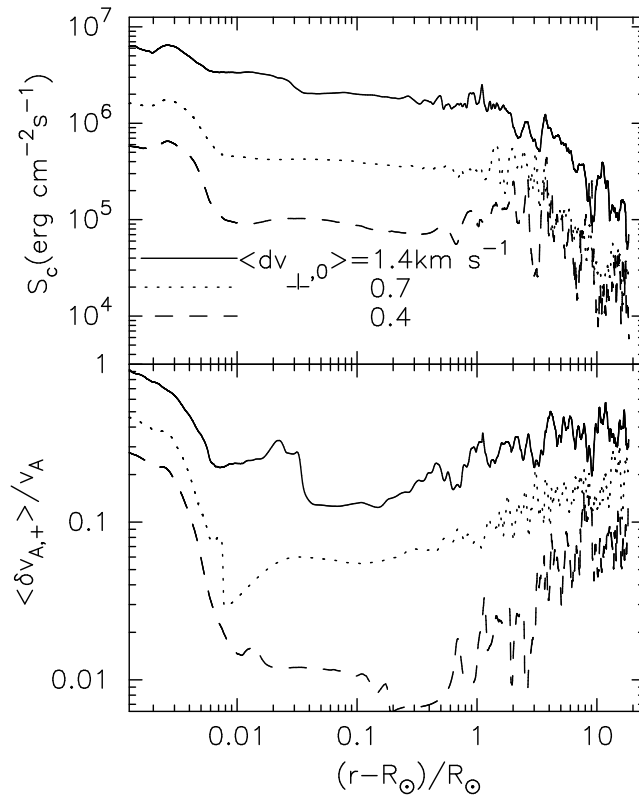


Figure 10. Same as Figure 6 but for different $\langle dv_{\perp,0} \rangle$. Solid, dotted, and dashed lines are results of $\langle dv_{\perp,0} \rangle = 1.4$ (Run VI), 0.7 (Run II), and $0.4(\text{km s}^{-1})$ (Run VII), respectively.

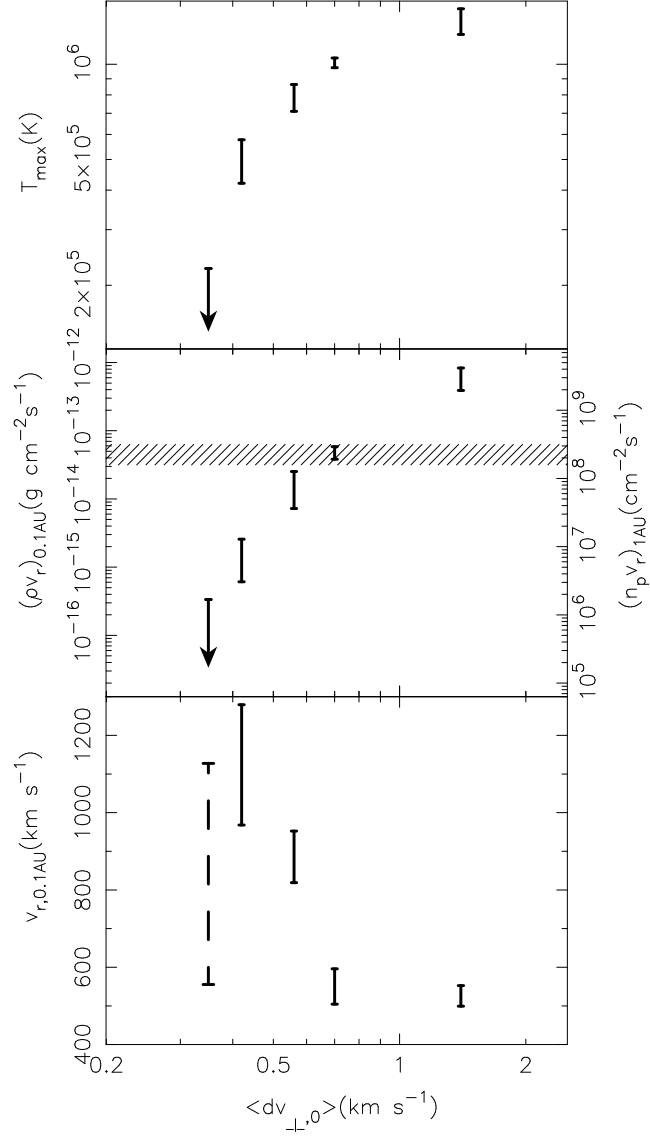


Figure 11. The maximum temperature, T_{\max} (K), (top), the mass flux of solar wind at 0.1AU, $(\rho v_r)_{0.1\text{AU}}$ ($\text{g cm}^{-2}\text{s}^{-1}$), (middle), and the solar wind speed at 0.1AU, $v_{r,0.1\text{AU}}$ (km s^{-1}) (bottom). On the right axis of the middle panel, we show proton flux at 1AU, $(n_p v_r)_{1\text{AU}}$ ($\text{cm}^{-2}\text{s}^{-1}$) estimated by assuming the solar elemental abundance. The shaded region in the middle panel is observed proton flux at 1AU. The upper limits in the top and middle panels for $\langle dv_{\perp,0} \rangle = 0.3\text{km s}^{-1}$ indicates that stable corona with the sufficient mass supply cannot be maintained and both T_{\max} and $(\rho v_r)_{0.1\text{AU}}$ decreases as the simulation proceeds. The wind speed also varies a lot, hence, the dashed error bar is used only for that case.

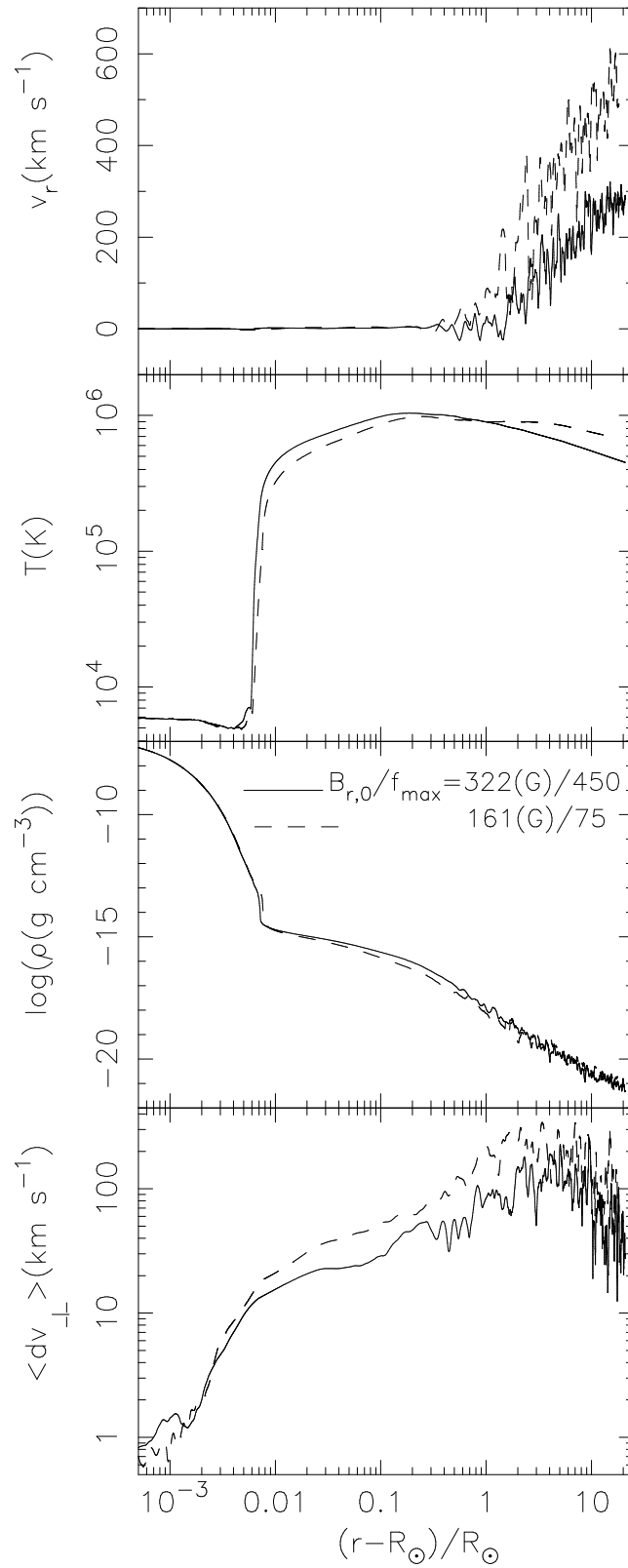


Figure 12. Same as Figure 5 but for different $B_{r,0}/f_{\max}$. Solid and dashed lines are results of $B_{r,0}(\text{G})/f_{\max} = 322/450$ (Run VIII) and $161/75$ (Run II), respectively.

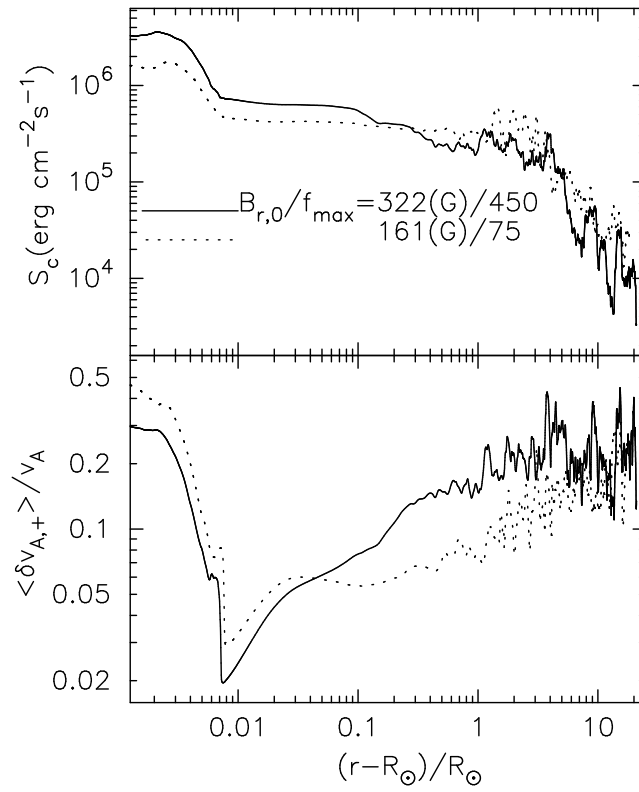


Figure 13. Same as Figure 6 but for different $B_{r,0}/f_{\max}$. Solid and dashed lines are results of $B_{r,0}(\text{G})/f_{\max} = 322/450$ (Run VIII) and $161/75$ (Run II), respectively.

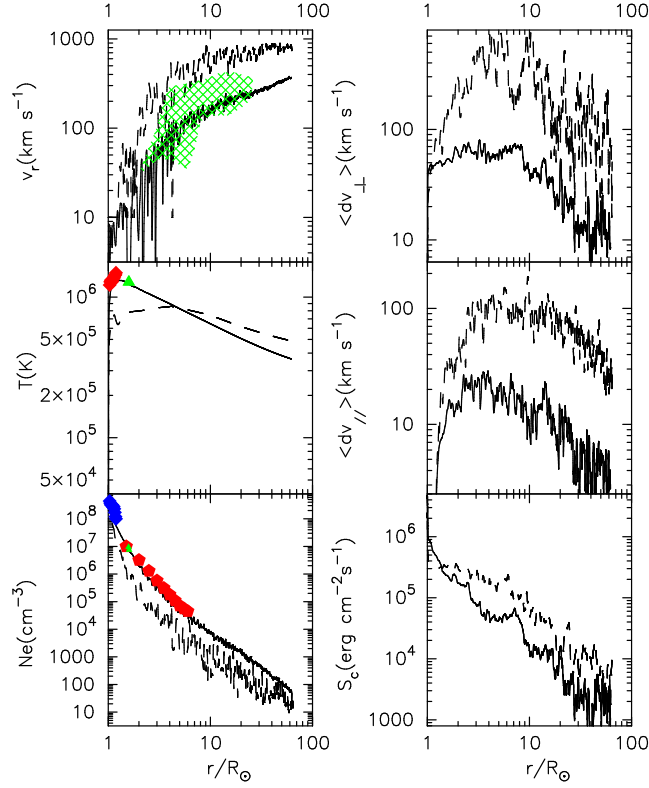


Figure 14. Simulation results of the slow (Run X; solid lines) and fast (Run I; dashed lines) solar wind models in comparison with slow-wind observations. On the left from top to bottom, outflow velocity, v_r (km s^{-1}), temperature, T (K), and electron density, N_e (cm^{-3}), are plotted with observation of mid- to low-latitude regions where the slow wind comes from. (see Figure 2 for the fast-wind observations). On the right from top to bottom rms transverse velocity, $\langle dv_{\perp} \rangle$ (km s^{-1}), rms longitudinal velocity, $\langle dv_{\parallel} \rangle$ (km s^{-1}), and the adiabatic constant, S_c ($\text{erg cm}^{-2} \text{s}^{-1}$) of the outgoing Alfvén waves are plotted. *Observational data; top-left* : Shaded region is observational data in the streamer belt [Sheeley et al., 1997]. *Middle-left* : Filled diamonds and triangles are electron temperature obtained from the line ratio of Fe XIII/X in the mid-latitude streamer by CDS/SOHO and UVCS/SOHO respectively [Parenti et al., 2000] *bottom-left* : Filled diamonds and triangles are data respectively from CDS and UVCS on SOHO observation of the mid-latitude streamer [Parenti et al., 2000], and filled pentagons derived from observation of the total brightness in the equator region by LASCO/SOHO [Hayes et al., 2001].

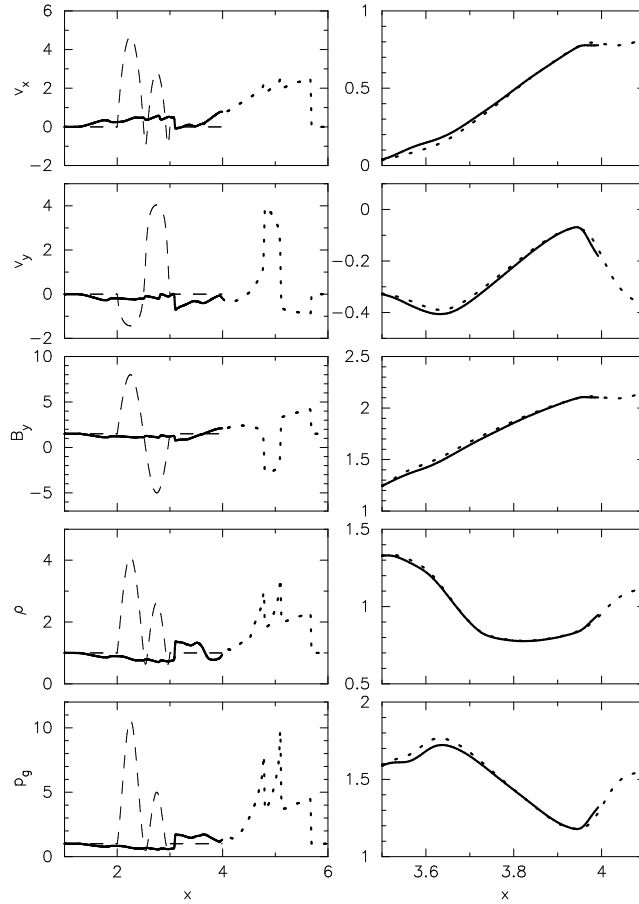


Figure 15. Reflection test for the oblique simple fast wave with $\delta v/v_f = 3.1$. From top to bottom, v_x , v_y , B_y , ρ , and p are plotted. In the panels on the right each quantity on the left is zoomed-up. Dashed and solid lines denote the initial and final ($t = 0.6$) states. Dotted lines are results of simulation in the broader region at $t = 0.6$. Differences between solid and dotted lines indicate errors due to our implementation of the outgoing boundary condition.

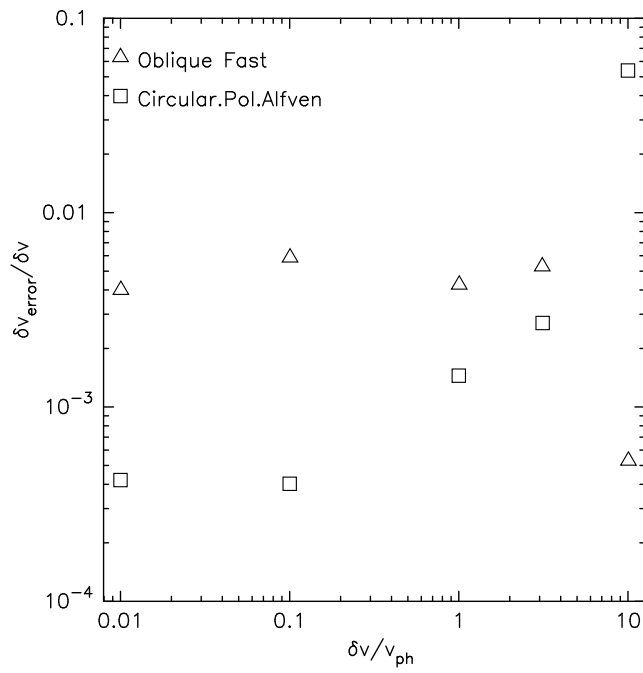


Figure 16. Reflection test for the simple fast and the Alfvén waves. Horizontal axis shows the input wave amplitudes normalized by the phase speed. Vertical axis plots errors due to our implementation of the outgoing boundary condition normalized by the input amplitude. (see text)